Comparison of CDF Electron Response between Test Beam and Simulation

Kostas Kordas
Department of Physics, McGill University
Montréal, Québec
Canada

A Thesis submitted to the
Faculty of Graduate Studies and Research
in partial fulfillment of the requirements for the degree of
Master of Science

Abstract

A comparison of the CDF (Collider Detector at Fermilab) central calorimeter electron response between 1991 test beam electron data and the CDF full detector simulation, using six variables that are used to identify electrons in CDF, is performed. Possible parameters that could be used to tune the simulation are also pointed out.

Résumé

Une étude de la réponse aux électrons du calorimètre central du CDF est effectuée. Elle consiste en une comparaison des réponses obtenues d' une part en 1991 à l' aide du faisceau d' électrons d' essai, et d' autre part grâce à une simulation de l' ensemble du détecteur, basée sur l' utilisation de six variables confirmant la présence d' électrons à l' intérieur du CDF. Enfin, un choix de paramètres devant permettre certains ajustements à la simulation est présenté.

Acknowledgements

I thank my supervisor Ken Ragan for giving me this project, for his guidance, patience and inspirational comments every time we had a discussion. I would also like to thank Klaus Strahl for the timely help he provided me over the last few months which proved crucial to the completion of this project. Special thanks to Yunling Ye who helped me sort out many a conceptual problem.

I am grateful to Dan Crane, Doug Benjamin and Brian Harral for helping me understand the CDF test beam.

Before I forget, thanks a lot you guys (Yunling, Niranjan, François, Graham, Alain, and David) for making our office a real fun place to work, not forgetting all my other friends outside work, especially Georgia, for their encouragement.

Lastly I thank my parents, brothers and sister back home and my relatives here in Montréal for their support during the course of this project.

Contents

List of Figures

List of Tables

Chapter 1

Introduction

1.1 Introduction

High energy physics deals with the study of the basic constituents of matter and the nature of interactions between them. In order to be able to look closely at such small-scale systems we need some kind of "microscope". The "microscope" that experimentalists in the field use, is nothing else but beams of high energy particles. High energies are important for two reasons:

> First, in order to localize the investigations to the very small scales of distance associated with the elementary constituents, one requires radiation of the smallest possible wavelength and so, highest possible energy.
>
> Second, many of the fundamental constituents have high masses and we must provide high enough energies for their creation and study.

Very high energy collisions occur naturally in cosmic ray interactions. They provide useful information but can not compare with systematic experimentation at accelerator laboratories.

When particle-1 in a high-energy beam meets particle-2 in a stationary target, their relative momentum k and their total energy E_{cm} in the center-of-mass frame are

$$E_{cm} = \sqrt{m_1^2 + m_2^2 + 2E_1 m_2} \approx \sqrt{2E_1 m_2}$$
$$k \approx \frac{1}{2}E_{cm} \tag{1.1}$$

assuming that $E_1 \gg m_1, m_2$. So, in order to get high E_{cm} with a fixed target, we need both high beam energy E_1 and substantial target mass m_2. However, E_{cm} increases only as the square root of E_1.

On the other hand, if particle-1 in one beam meets particle-2 in another beam moving in the opposite direction, the available energy becomes

$$E_{cm} = \sqrt{m_1^2 + m_2^2 + 2E_1E_2 + 2p_1p_2} \approx \sqrt{4E_1E_2} \tag{1.2}$$

where p_1, p_2, E_1, E_2 are the two beam momenta and energies and $k \approx \frac{1}{2}E_{cm}$ as before. The particle masses can now be very low. But, most important, E_{cm} rises linearly with the beam energies, assuming both are increased together.

One of the most active accelerator laboratories today is Fermilab at Batavia near Chicago. There, both fixed target and collider experiments are carried out.

In the collider mode the acceleration ring (the Tevatron) collides 900 GeV protons with 900 GeV anti-protons, providing a center-of-mass energy $\sqrt{s} = 1.8$ TeV, the highest energy available in the field today. The first detector built for the Tevatron collider is CDF (Collider Detector at Fermilab) which is located at the $B0$ interaction region of the Tevatron ring.

1.2 Physics at CDF

A broad range of physics prospects is available at CDF: heavy quark production and decay, W and Z physics, QCD and jet physics, and searches for exotic particles.

In the Standard Model the top quark (t) is predicted to be the weak isospin partner of the bottom quark (b). Its existence is implied by the absence of flavor-changing neutral currents in b decays [1] and the forward-backward asymmetry in $e^+e^- \rightarrow b\bar{b}$ interactions [2]. At the Tevatron, the dominant production mechanism is expected to be $\bar{p}p \rightarrow t\bar{t}X$, where X is anything. An important goal for CDF would be to find the top quark. For the moment CDF has set the lower limit for the top quark mass to be 91 GeV/c^2 at a 95% confidence level [3].

There are many $B - \overline{B}$ pairs produced in the Tevatron collider, and so CDF is able to explore B-physics too. Measurements of the $B^0\overline{B^0}$ mixing parameter χ have been done with CDF [4]. The phenomenon of mixing, in which a neutral meson transforms into its antiparticle via flavor-changing weak interactions, provides constraints on the elements of the Cabbibo-Kobayashi-Maskawa matrix. Full reconstruction of B mesons through decay chains like $B^\pm \rightarrow J/\psi K^\pm, J/\psi \rightarrow \mu^+\mu^-$ have also been done at CDF and the obtained data samples have been used to measure B-meson cross sections, from which the b-quark cross section has been extracted [5].

The masses m_W and m_Z of the vector bosons are fundamental parameters in the standard electroweak model. Together they determine the weak mixing angle through its definition, $sin^2\theta_W \equiv 1 - m_W^2/m_Z^2$ which can be compared to determinations made using other methods, thus testing the consistency of the model. The W mass is measured using both electron and muon decays of the W ($W \to e\nu, \mu\nu$) [6], and the Z mass using the $Z \to e^+e^-, \mu^+\mu^-$ data [7].

QCD can be tested with jets and isolated prompt photons that are produced at the $B0$ interaction point, in contrast to photons produced by decays of hadrons. To test QCD with jets, the inclusive jet cross section ($\bar{p}p \to j + X$, where j stands for jet and X for anything) is compared to QCD predictions [8]. Additional information about QCD and limits on quark compositeness can be obtained from two jet angular distributions ($\bar{p}p \to jj + X$) and their comparison to QCD predictions [9]. The cross section for the production of prompt photons can also be compared to QCD [10]. So far, measurements of jets at CDF agree with QCD, whereas measurements of isolated prompt photons do not agree with QCD calculations at low momentum.

Apart from the above, searches for W' and Z', excited states of the charged and neutral vector bosons W and Z respectively [11], for squarks and gluinos, the supersymmetric (SUSY) partners of quarks and gluinos respectively [12], for a light Higgs boson ($m_H < 1$ GeV/c^2) [13], as well as for heavy stable charged particles [14] are done at CDF.

1.3 The CDF detector

The CDF detector (see Fig. 1.1) is a general purpose magnetic detector with charged particle tracking and momentum determination, fine-grained electromagnetic and hadronic calorimetry, and electron and muon identification. For a detailed description of the detector refer to [15]. Here we briefly outline its main features.

The CDF coordinate system defines the positive z axis along the direction traveled by the protons. The y axis is vertically upward and the x axis is radially outward from the center of the Tevatron ring. The CDF detector is forward-backward symmetric. The angles θ and ϕ are the usual polar and azimuthal angles. Pseudorapidity, $\eta = -\ln\tan(\theta/2)$, is a polar angle variable widely used at CDF[1]. The variable r is the perpendicular distance to the beam ($r = \sqrt{x_{CDF}^2 + y_{CDF}^2}$). We often use the "transverse" energy, $E_T \equiv E \cdot sin\theta$, and the "transverse" momentum, $p_T \equiv p \cdot sin\theta$,

[1]Whenever a coordinate x, y, z, ϕ, θ or η is used as the CDF detector coordinate, the notation will be $x_{CDF}, y_{CDF}, z_{CDF}, \phi_{CDF}, \theta_{CDF}$ or η_{CDF}, with $x_{CDF} = y_{CDF} = z_{CDF} = 0$ at the intersection point between the nominal beam line and the plane where the detector is forward-backward symmetric.

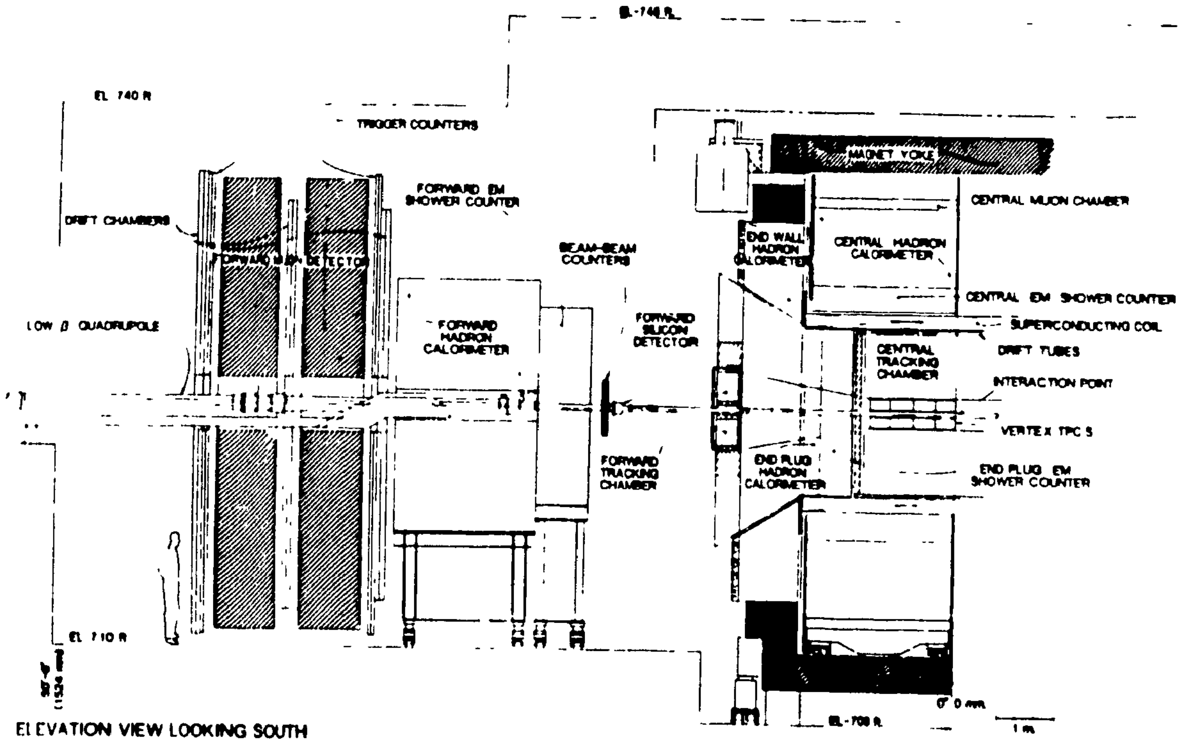

Figure 1.1: A side view of one half of the CDF detector as it was configured for the 1988– '89 run. A new vertex time projection tracking system (VTX) has replaced the VTPC (vertex time projection chamber), a silicon vertex detector has been installed between the beam pipe and the VTX, and new muon chambers have been implemented for the 1992– '93 run. The detector is symmetric about the $\eta_{CDF} = 0$ plane.

where E is the energy measured in the calorimeter and p is the momentum of the track.

1.3.1 Tracking

Immediately outside of the beryllium beam pipe, a silicon vertex detector (SVX), made of 4 layers of silicon crystals at distances of minimum approach $r = 3.0, 4.3, 5.7,$ and 7.9 cm and having 46080 channels in total, covers the region $|z_{CDF}| \leq 26$ cm ($|\eta_{CDF}| \leq 1.9$ for layer 4). The primary function of the SVX is to find secondary vertices, needed for B meson reconstruction and also for top decays. The SVX has a vertex/impact parameter resolution of $\approx 10\mu$m, well suited to identify secondary vertices of relatively long lived particles (e.g. B mesons).

Outside of the SVX barrels, a system of twenty-eight time projection vertex drift chambers (the VTX) are used to provide tracking information for $|\eta_{CDF}| \leq 3.5$, giving good coverage of the long interaction region ($\sigma_z \approx 35$ cm). The VTX chambers contain 8412 sense wires for measurement of track coordinates projected onto the $r - z$ plane and there is also a much poorer measurement in ϕ to provide stereo information. The primary function of the VTX is to locate the event vertex along the beam axis. The resolution of this measurement is $\approx 1 - 2$ mm, depending on the track multiplicity. Another function of the VTX is to provide information used in the identification of photon conversions.

At larger radii, the central tracking chamber (CTC) provides charged particle tracking for $|\eta_{CDF}| \leq 1.1$, above $p_T \approx 300$ MeV/c. Track curvature is measured in a uniform 1.4 T solenoidal magnetic field coaxial with the beam axis. The CTC is a large cylindrical drift chamber with an outer radius of 1.4 m and contains 84 layers of sense wires grouped into 9 "superlayers". Five of these superlayers consist of 12 axial sense wire layers; the other four superlayers consist of six layers of sense wires tilted by $\pm 3°$ relative to the beam direction. The track measurement provides a momentum resolution of r.m.s$(p_T)/p_T^2 \leq 0.002$ (GeV/c)$^{-1}$ for isolated charged tracks, where r.m.s(p_T) stands for the root mean square of the p_T distribution. The resolution can be improved to r.m.s$(p_T)/p_T^2 \leq 0.0011$ (GeV/c)$^{-1}$ by constraining track trajectories to pass through the beam position.

1.3.2 Calorimetry

One of the basic inputs to the CDF triggers is based on the energy sum in the calorimeter. In high energy proton-antiproton collisions most of the energy deposited in the calorimeters is due to clusters of hadrons traveling in a relatively small solid angle (jets), or due to electrons that deposit their energy in a much smaller solid angle than the jets. A projective tower geometry was chosen for all calorimeters in order to contain a jet or an electron within the same towers from the start to the end of its traveling in the calorimeter. This way the electrons deposit their energy in a much smaller number of towers than the jets, and it is easy for the trigger to distinguish between a jet and an electron.

Each tower has an electromagnetic (EM) calorimeter cell in front of a corresponding hadronic one (HAD). This enables a detailed comparison of electromagnetic and hadronic energy on a tower-by-tower basis. The division between EM and HAD sections helps in distinguishing between electromagnetic showers ($e^{\pm}, \gamma$) and hadronic showers, because incident electrons or photons will deposit almost all of their energy in the EM part of the calorimeter, whereas hadrons will deposit a large portion of

System	η_{CDF} range	Energy resolution ($\sigma(E)/E$)	Thickness
CEM	$\lvert\eta\rvert < 1.1$	$13.5\%/\sqrt{E} \oplus 2\%$	$18X_0$
PEM	$1.1 < \lvert\eta\rvert < 2.4$	$28\%/\sqrt{E} \oplus 2\%$	$18 - 21X_0$
FEM	$2.4 < \lvert\eta\rvert < 4.2$	$25\%/\sqrt{E} \oplus 2\%$	$25X_0$
CHA	$\lvert\eta\rvert < 1.3$	$75\%/\sqrt{E} \oplus 3\%$	$4.5\lambda_I$
PHA	$1.3 < \lvert\eta\rvert < 2.4$	$90\%/\sqrt{E} \oplus 4\%$	$5.7\lambda_I$
FHA	$2.4 < \lvert\eta\rvert < 4.2$	$130\%/\sqrt{E} \oplus 4\%$	$7.7\lambda_I$

Table 1.1: Summary of the CDF calorimeter properties. The symbol $\oplus$ means that the two terms should be added in quadrature (energy is in GeV).

their energy in the HAD part of the calorimeter behind the corresponding EM section.

The CDF calorimeters are divided into three regions of pseudorapidity: central ($|\eta_{CDF}| \leq 1.1$), plug ($1.1 \leq |\eta_{CDF}| \leq 2.4$), and forward ($2.4 \leq |\eta_{CDF}| \leq 4.2$). The dimensions of the towers are $\Delta\eta \times \Delta\phi \approx 0.1 \times 15°$ in the central region and $\Delta\eta \times \Delta\phi \approx 0.1 \times 5°$ in the plug and forward regions.

The EM calorimeter cells are constructed from active sampling layers sandwiched between lead radiator plates. The active layers are scintillators in the central region (CEM calorimeter) and gas proportional chambers in the plug (PEM calorimeter) and the forward (FEM calorimeter) regions. In the CEM calorimeter a set of proportional strip chambers is located at a depth of ≈ 6 radiation lengths, corresponding to the depth of maximum energy deposition in an electromagnetic shower. These central strip chambers (CES) have wire and strip readout providing independent reconstruction of showers in the z and ϕ views, measure the lateral shape and position of EM showers and are used for electron and photon identification. The electromagnetic showers are located with a precision of $\approx \pm 2$ mm depending on the shower energy.

The hadron calorimeter cells also use scintillator as the active medium in the central (CHA calorimeter) and the end-wall (WHA calorimeter) regions ($|\eta_{CDF}| \leq 1.3$). The active medium is gas proportional chambers for the plug (PHA) and the forward (FHA) hadronic calorimeters. In both cases the active layers are sandwiched between iron absorbers. The CHA/WHA photomultiplier tubes (PMTs) are instrumented with TDCs that provide timing information used to reject out-of-time backgrounds, such as cosmic rays or particles from the original Fermilab accelerator, that is now used as an injector for the Tevatron and which passes over the CDF detector. In Table 1.1, the η coverage, the energy resolution and the depth in radiation (X_0) or interaction lengths (λ_I) for the EM/HAD calorimeters are summarized. The radiation length is the distance an electron has to travel on average before it is left with $1/e$ of its initial energy due to bremsstrahlung, and the interaction length characterizes the inelastic production of secondary hadrons.

1.3.3 Muon detection

The region of the outermost part of the central calorimeter with $|\eta_{CDF}| \leq 0.63$ i.e. $56° \leq \theta_{CDF} \leq 124°$, is instrumented with four layers of drift chambers for muon detection (the CMU detector). The central calorimeter (CEM + CHA) has a thickness of ≈ 5 interaction lengths (λ_I). So, muons of momenta below approximately 1.6 GeV/c stop in the calorimeter without reaching the CMU whereas the CMU is maximally efficient for muon momenta above approximately 3 GeV/c. Muon identification is done by matching a track segment in the CMU with a CTC track. The root mean square (r.m.s) position resolution along the sense wires is 1.2 mm (using charge division information), and the r.m.s resolution in the drift direction (ϕ) is 250 μm. In both the forward and backward regions, between 3° and 16° relative to the beam axis, there is a muon spectrometer (FMU) consisting of magnetized steel toroids with drift-chamber planes and trigger scintillation counters. The position resolution is 130 μm.

After 60 cm of steel outside the CMU, four layers of chambers are located; the central muon upgrade (CMP) detector. The 60 cm of steel increase the number of interaction lengths to ≈ 8.5, between the beam collision point and the CMP chambers. This reduces the rate of non-interacting primary hadrons ("punch-throughs") by a factor of 20. The position resolution of the CMP is ≈ 295 μm and the angular resolution (in ϕ) is ≈ 4.6 mrad.

Additional muon coverage for $0.62 \leq |\eta_{CDF}| \leq 1.0$ is provided by the central muon extension (CMX) detector. It consists of four layers of drift chambers located after approximately $4\lambda_I$ of absorber. The CMX drifts cells are similar to the CMP ones and the position and angular resolutions are the same.

Chapter 2

The CDF Central Calorimeter and Electrons

2.1 Calorimetry in High Energy Physics

A calorimeter is a block of matter that intercepts a particle and causes it to interact and deposit most of its energy within the calorimeter volume by a cascade (or "shower") of lower and lower energy particles. The energy deposited is detected in the form of scintillator light, ionization charge or similar, produced by the secondary particles in the shower. The energy detected is, if the system is carefully designed, proportional to the energy of the incident particle. Calorimeters are used in high energy physics to measure energy, position, direction and sometimes the nature of incident particles (e.g distinguish between an electron and a charged pion).

2.1.1 Sampling calorimeters

"Sampling" calorimeters are devices where the functions of energy degradation and energy measurement are separated in alternating layers of passive and active material. This is done so as to avoid using only active materials, which are usually of low atomic number (Z) or expensive materials. By introducing the high Z passive materials we cause the shower to develop faster and so we can reduce the volume of the calorimeter.

Of course the combined use of passive and active materials means that we are not measuring all the energy deposited in the calorimeter (both in the passive and the active parts), but only the energy deposited in the active parts. So we have "sampling fluctuations"[16] which are mainly caused because there are statistical fluctuations on the number of secondary particles, N, going through the active layers. These sampling fluctuations have a fractional resolution $\sigma(E)/E$ that scales as $1/\sqrt{N} \sim 1/\sqrt{E}$. Note also that fluctuations would be present even in a calorimeter made up by pure active material, because every material is sensitive to the cascade particles above some cut-off energy, so there is always some energy that is going to be missing ("intrinsic" fluctuations). Intrinsic fluctuations scale as $\sigma(E)/E \sim 1/\sqrt{E}$.

Other effects that cause fluctuations are Landau fluctuations of the energy deposited in the active layers (a significant amount of energy, well above the average value, can be lost by a particle in a single collision), "path-length" fluctuations, fluctuations due to energy leakage out of the calorimeter, etc.

2.1.2 Electromagnetic and hadronic showers

When a high-energy electron/photon enters a thick absorber it creates an electromagnetic shower by bremsstrahlung/pair production. The multiplication process of the shower goes on until the shower particles reach a threshold energy; from then on no new particles are created and the existing ones lose their energy gradually by collision-ionization losses (electrons) or by Compton scattering and the photoelectric effect (photons).

It is convenient to measure the thickness of the material where the electromagnetic cascade develops, in units of the radiation length X_0. This is the distance an electron has to travel on average before being left with $1/e$ of its initial energy. The threshold energy where collision losses become as important as losses due to bremsstrahlung is called the critical energy E_c. The average lateral deflection of electrons of energy E_c after traveling for one radiation length is the 'Molière Radius' R_M. Radiation length, critical energy and Molière radius, for a material with atomic weight A and atomic number Z, can be parametrized as follows (ref. [16] for E_c and R_M, ref. [17] for X_0):

$$
\begin{aligned}
X_0 &\approx \frac{716.4\ A}{Z(Z+1)\ \ln(287/\sqrt{Z})}\ \ [\frac{g}{cm^2}] \\
E_c &\approx \frac{550}{Z}\ \ [MeV] \\
R_M &\approx 7\frac{A}{Z}\ \ [\frac{g}{cm^2}]
\end{aligned}
\tag{2.1}
$$

where the above formulas are accurate to better than 10% for E_c and R_M for materials with $13 \leq Z \leq 92$, and to better than 2.5% for X_0 for all elements except helium, where the result is $\approx$ 5% low. Notice that if we want to convert X_0 or R_M to distance, we have to divide by the density of the medium.

As concerns the longitudinal development of the shower, the deposited energy can be parametrized as follows, with a and b as parameters ([18],[19]):

$$\frac{dE}{dt} = E_0 \frac{b^{a+1}}{\Gamma(a+1)} t^a e^{-bt} \tag{2.2}$$

where t is the number of radiation lengths traversed from the shower origin and E_0 is the total particle energy.

The calorimeter length needed to contain 98% of the incident energy is $L(98\%)$ ([18]):

$$\begin{aligned} L(98\%) &\approx t_{max} + 4\lambda_{att} \\ t_{max}[X_0] &= a/b \\ \lambda_{att}[X_0] &\approx 3.4 \pm 0.5 \end{aligned} \tag{2.3}$$

where λ_{att} characterizes the slow exponential decay of the shower after the shower maximum, and t_{max} is the depth at which the maximum of the shower occurs.

As concerns the lateral development of the shower (mainly due to multiple scattering and the bremsstrahlung emission angle), 95% of the total energy of the shower is contained in a cylinder having radius $R(95\%)$[16].

$$R(95\%) \approx 2R_M \approx 14\frac{A}{Z} \ \left[\frac{g}{cm^2}\right] \tag{2.4}$$

Unlike the electromagnetic showers, hadronic showers are composed of both an electromagnetic part (mainly due to π^0's created in one of the first interactions of the hadron in the calorimeter) and a hadronic part. In general these energy depositions are converted to electric signals with different efficiencies. This is because a significant part of the low energy hadronic component is invisible (going to excite or to break-up nuclei of the traversed medium). The ratio of the conversion efficiencies is called the intrinsic e/h ratio. In most cases the e/h ratio is usually greater than unity (typical values are $e/h \approx 1.4$ for most materials[1], which is also the case for the CDF central calorimeter). The e/h ratio increases as the energy of the incoming hadron increases, because the electromagnetic portion of the shower is greater than at lower energies (the fraction of the π^0's in a hadronic shower is $f(\pi^0) \approx 0.1\,\mathrm{lnE(GeV)}$ [18]).

The length scale appropriate for hadronic cascades is the nuclear interaction length (or absorption length) given by ([18]):

$$\lambda_I \approx 35A^{\frac{1}{3}} \ \left[\frac{g}{cm^2}\right] \tag{2.5}$$

[1]With the exception of Uranium-238 which boosts the hadronic component to achieve $e/h \approx 1$

Quantities describing the longitudinal and the lateral development of hadronic showers, similar to the ones used for electromagnetic showers, can also be defined ([18]).

2.2 The CDF central calorimeter

The CDF central calorimeter is a sampling calorimeter divided into two regions, electromagnetic (CEM) [20] and hadronic (CHA) [21]. The passive medium in the electromagnetic part is lead, whereas in the hadronic part it is iron. The active medium is in both cases scintillator. The electromagnetic part is located in front of the hadronic one, since the radiation length (X_0) is much shorter than the interaction length (λ_I) and so electrons and photons produce electromagnetic showers much earlier than hadrons in the calorimeter. The depth of the electromagnetic part is $18X_0$ so as to contain most of the electromagnetic shower (see eq. 2.3), and the depth of the hadronic part is $4.7\lambda_I$ for the same reason. Note that the energy resolution of the EM calorimeters is affected significantly by the energy lost due to inadequate containment of the showers in the calorimeter volume, since the intrinsic resolution of such calorimeters is small; thus the $18X_0$ of the CEM depth. On the other hand the measurement of the jet energy need not be that precise as that of electrons. Also size considerations of the hadronic calorimeters along with hadronic shower containment experiments for iron calorimeters, show that $\approx 5\lambda_I$ are sufficient for the CHA.

The central calorimeter provides full ϕ coverage and, in order to make mechanical construction easier and to be able to roughly locate incoming particles, it is divided into 48 wedges, each covering $\Delta\phi_{CDF} = 15°$. The wedges are grouped into 4 arches. Two arches (12 wedges each) cover the positive η_{CDF} ($z_{CDF} > 0$) region and two arches cover the negative η_{CDF} ($z_{CDF} < 0$) region for $|\eta_{CDF}| < 1.1$. Each wedge is divided into a number of towers; the size of each tower is $\Delta\eta_{CDF} \times \Delta\phi_{CDF} \approx 0.1 \times 15°$. An electromagnetic shower is mostly contained within one tower (recall the 'Molière Radius' R_M and eq. 2.4. For the CEM, $R_M = 3.53$ cm). The towers have a projective geometry pointing to the interaction region, so as to contain a jet inside the same towers from the start to the end of its showering inside the central calorimeter. Each wedge contains 10 towers for the CEM part of the calorimeter. Due to this projective geometry the CHA has only 8 towers per wedge and so the region behind the CEM towers at $|\eta_{CDF}| \approx 1$ is also covered by the "wall" hadronic calorimeter (WHA). The CHA and WHA combined cover the region $|\eta_{CDF}| < 1.3$ (see Fig. 2.1). Notice that the CEM towers connect smoothly to the PEM (plug electromagnetic calorimeter)

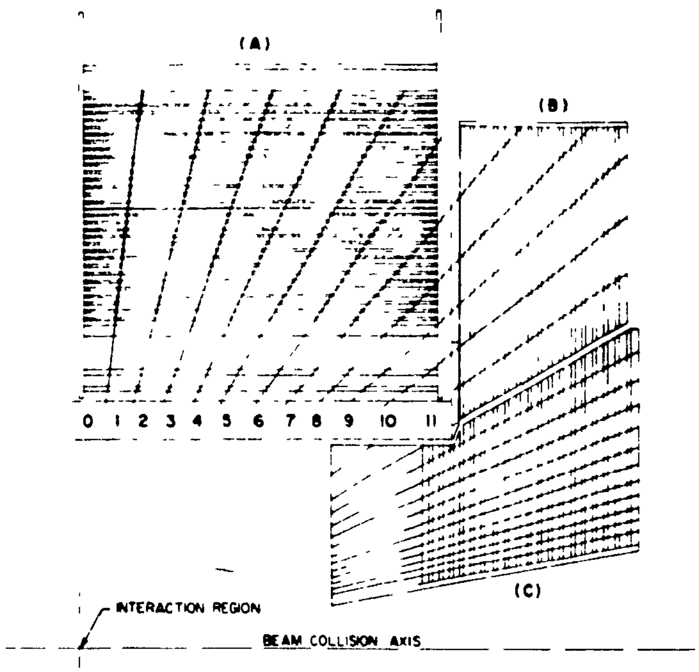

Figure 2.1: Quadrant of the calorimeter where A, B, C show central, endwall and plug respectively. Towers are numbered from 0 (at $\theta_{CDF} = 90°$) to 11 (last tower of endwall modules). Hadronic towers 6, 7 and 8 are shared between central and endwall calorimeter.

towers and so there is no need for a "wall" electromagnetic calorimeter.

The light from the scintillator layers is collected in a different manner in CEM than in CHA (see Fig. 2.2). In the CEM, there is one wavelength shifter (WLS) sheet at each ϕ-side of the tower, collecting the light from all the 31 scintillator layers in a CEM tower. In the CHA, there are two WLS strips collecting light from the long ϕ-sides of each of the 32 scintillator layers in a CHA tower. In both cases the (WLS) sheets (for CEM) or strips (for CHA) pass the light, through light guide strips, to the photomultiplier tubes (PMTs). There are two PMTs per CEM tower and two more for each CHA tower, at opposite sides in ϕ.

Each ϕ-side of a wedge is covered by $\approx$ 4.76 mm of steel skin and between the wedges there are ϕ gaps of size $\approx$ 6.4 mm. Steel skins and gaps represent 4.8% of the azimuth. In order to avoid having photons or electrons traverse the ϕ gaps and escape detection, there are crack detectors in the ϕ boundaries consisting of a preradiator (9 radiation length thick uranium bars which forces the incoming particles to shower) and a crack proportional chamber which detects particles going through the cracks. The information from the crack detectors is used for veto purposes. Note that by wedge design (due to the steel skins and the ϕ-gaps) an electromagnetic shower does not have significant energy deposition to the wedges neighbouring the hit wedge.

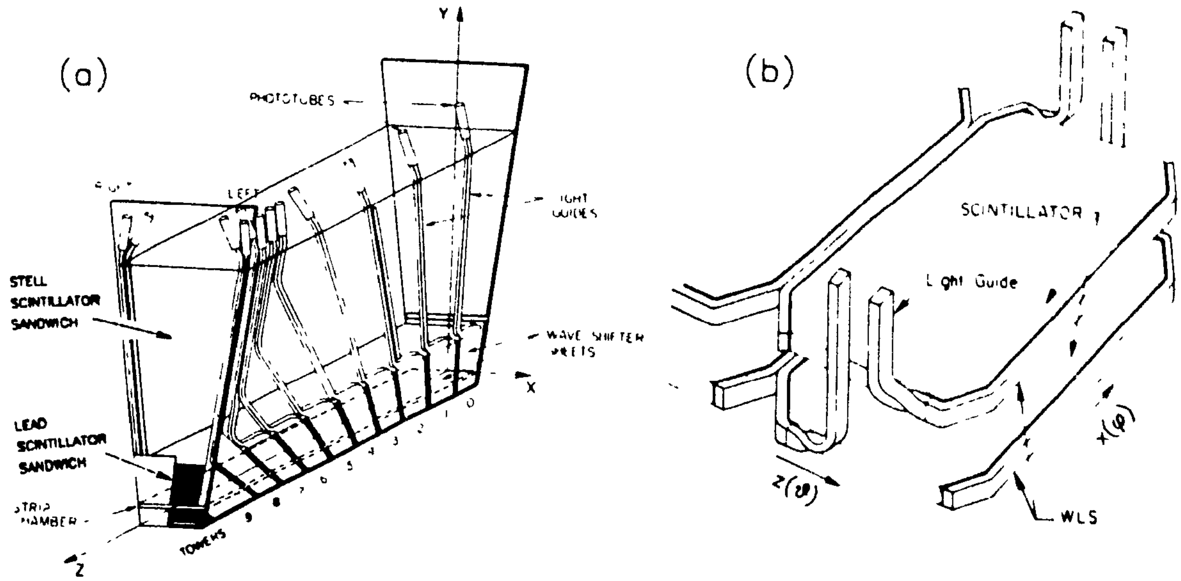

Figure 2.2: The light gathering system for the CEM (a) and the CHA (b). The local wedge coordinate system is also shown in (a).

At a depth of $\approx 5X_0$ from the face of the CEM towers (a little more than $6X_0$ from the interaction point including the detector and solenoid coil material up to the CEM face[2]), strip chambers (CES) are located. Their location is chosen so as to correspond to the maximum of the electromagnetic showers (see eq. 2.3). The strip chambers determine the position and the transverse development of the showers by measuring the deposition of charge on orthogonal strips and wires. Thus, both ϕ (using the wires) and z coordinates (using the strips) of the showers are obtained. The electromagnetic showers are located with a precision of $\approx \pm 2$ mm (at 50 GeV) depending non-linearly on the shower energy (see Fig. 2.3).

The energy resolution for the electromagnetic and the hadronic component of the central calorimeter are:

$$\frac{\sigma(E)}{E} \approx \frac{13.5\%}{\sqrt{E}} \oplus 2\% \qquad \text{(CEM)}$$
$$\frac{\sigma(E)}{E} \approx \frac{75.0\%}{\sqrt{E}} \oplus 3\% \qquad \text{(CHA)} \tag{2.6}$$

where E is the energy measured in the calorimeter in GeV, and the symbol $\oplus$ means that the two terms should be added in quadrature. The poorer resolution of the hadronic part is due to the different natures of the electromagnetic and hadronic showers (recall end of section 2.1.2).

[2]About 85 % of this extra $1X_0$ is at the solenoid coil.

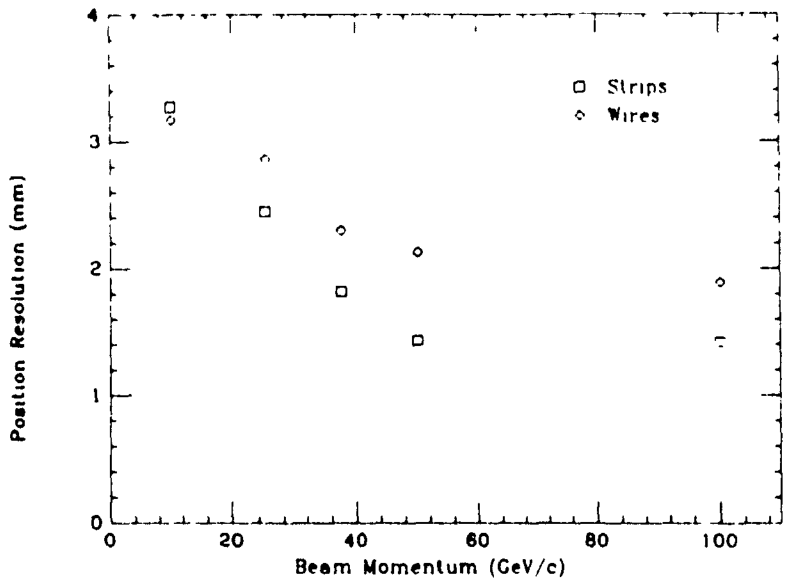

Figure 2.3: Strip chamber position measurement resolution near $\theta_{CDF} = 90°$. Strip view (squares) measurement scales as $1/sin\theta$ away from $\theta_{CDF} = 90°$.

2.3 Electrons in the CDF central calorimeter

In the central calorimeter, electrons are identified by requiring that there be an electromagnetic cluster in the CEM and an associated track in the CTC. The cluster must have a shower profile in agreement with 1985 test beam results for electrons, both in the calorimeter and the strip chambers (CES). In addition the track must match the cluster in momentum (an electron will deposit all of its energy inside the calorimeter, most in CEM and sometimes a small fraction in the CHA) and position (i.e the CTC track must point to the electromagnetic cluster).

An electromagnetic cluster is usually defined as a cluster of energy located at a tower with energy greater than 3 GeV ("seed" tower). If adjacent towers have energy greater than 0.1 GeV they are considered as part of the electromagnetic cluster. Because electromagnetic showers have very small energy leakage across the ϕ boundaries, the size of such a shower extends to no more than 3 η -adjacent towers.

The variables used to parametrize an electromagnetic shower and used for a more detailed selection are:

• E_{CHA}/E_{CEM}, where E_{CHA} is the energy measured in CHA and E_{CEM} the energy measured in the CEM. The usual convention for the E_{CEM} energy is to count the energy in the 3 η-adjacent CEM towers that contain the electromagnetic shower, and for the E_{CHA} energy to count the energy in the 3 CHA towers behind these 3 CEM towers.

• L_{SHR}, that parametrizes the lateral shower profile of the energy spread of the cluster. The energies of the towers adjacent to the seed towers are compared to expectations based on 1985 test beam results for electrons. The actual definition for L_{SHR} is:

$$L_{SHR} = 0.14 \sum_k \frac{M_k - P_k}{\sqrt{0.14^2 E_{CEM} + (\Delta P_k)^2}} \tag{2.7}$$

where the sum is over towers in the cluster adjacent to the seed tower, M_k is the measured energy in the adjacent tower, P_k is the expected energy in the adjacent tower as estimated from 1985 test beam measurements, E_{CEM} is the electromagnetic energy in the cluster, and ΔP_k is an estimate of the error in P_k; the first term in the denominator comes from the resolution of the CEM.

• χ^2_z and χ^2_ϕ, which characterize the fit of the transverse profiles of the cluster in the z and ϕ directions, to a parametrization of the profiles obtained from 1985 test beam electrons[22].

• E/P, where E is the energy measured in the calorimeter (CEM + CHA) and P is the momentum as measured in the CTC tracking chamber.

• Δz and Δx, which are defined as follows:

$$\begin{aligned} \Delta z &= z_{CES} - z_{CTC} \\ \Delta x &= x_{CES} - x_{CTC} \end{aligned} \tag{2.8}$$

where z_{CES} and x_{CES} are the z and x location of the electromagnetic shower according to the strip chambers, and z_{CTC} and x_{CTC} are the extrapolated position of the electron to the radius of the strip chambers, using the corresponding CTC track. The z and x coordinates here are the local wedge coordinates (see Fig. 2 2(a)). The local z-axis is identical to the CDF z-axis (pointing towards the direction of beam protons), the local x-axis is in the direction of the azimuthal (i.e ϕ) tangent at the tower center, pointing towards the lower ϕ values, and the local y-axis is perpendicular to the face of the wedge pointing outwards, such that the local coordinate system is right handed. So, in local coordinates, $x = 0$ is at the tower center and $y = 0$ on the front face of the CES. The coordinates of the CEM towers are given in table 2 1.

An application of electron identification using cuts on the values of the above variables is demonstrated in Fig. 2.4 [23]. Schematic views of an electron, a muon and a charged pion in the central calorimeter are given in Fig. 2.5 [24].

Tower	z_{min} (cm)	z_{max} (cm)	η_{min}	η_{max}
0	4.22	24.16	0.023	0.131
1	24.16	48.32	0.131	0.260
2	48.32	72.48	0.260	0.384
3	72.48	96.64	0.384	0.503
4	96.64	120.80	0.503	0.616
5	120.80	144.96	0.616	0.723
6	144.96	169.12	0.723	0.823
7	169.12	193.28	0.823	0.916
8	193.28	217.44	0.916	1.004
9	217.44	245.96	1.004	1.100

Table 2.1: Horizontal (z) coordinates of the CEM towers. The vertical (ϕ) coordinates run from n $\times$ 15° to (n + 1) $\times$ 15°, where n = 0, 1, ..., 23 is the wedge number.

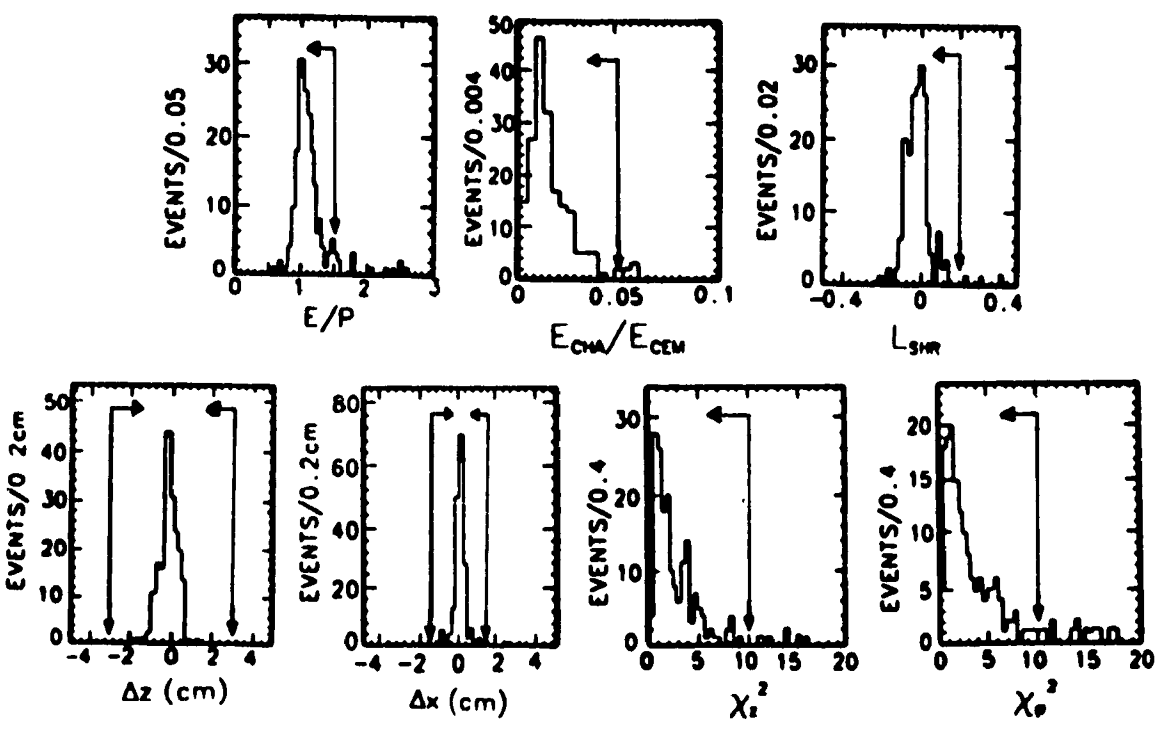

Figure 2.4: Standard CDF cuts used for electron identification: $E/P < 1.5$, $E_{CHA}/E_{CEM} < 0.05$, $L_{SHR} < 0.2$, $|\Delta z| < 1.5$ cm, $|\Delta x| < 3$ cm, $\chi_z^2 < 10$ and $\chi_\phi^2 < 10$ [23].

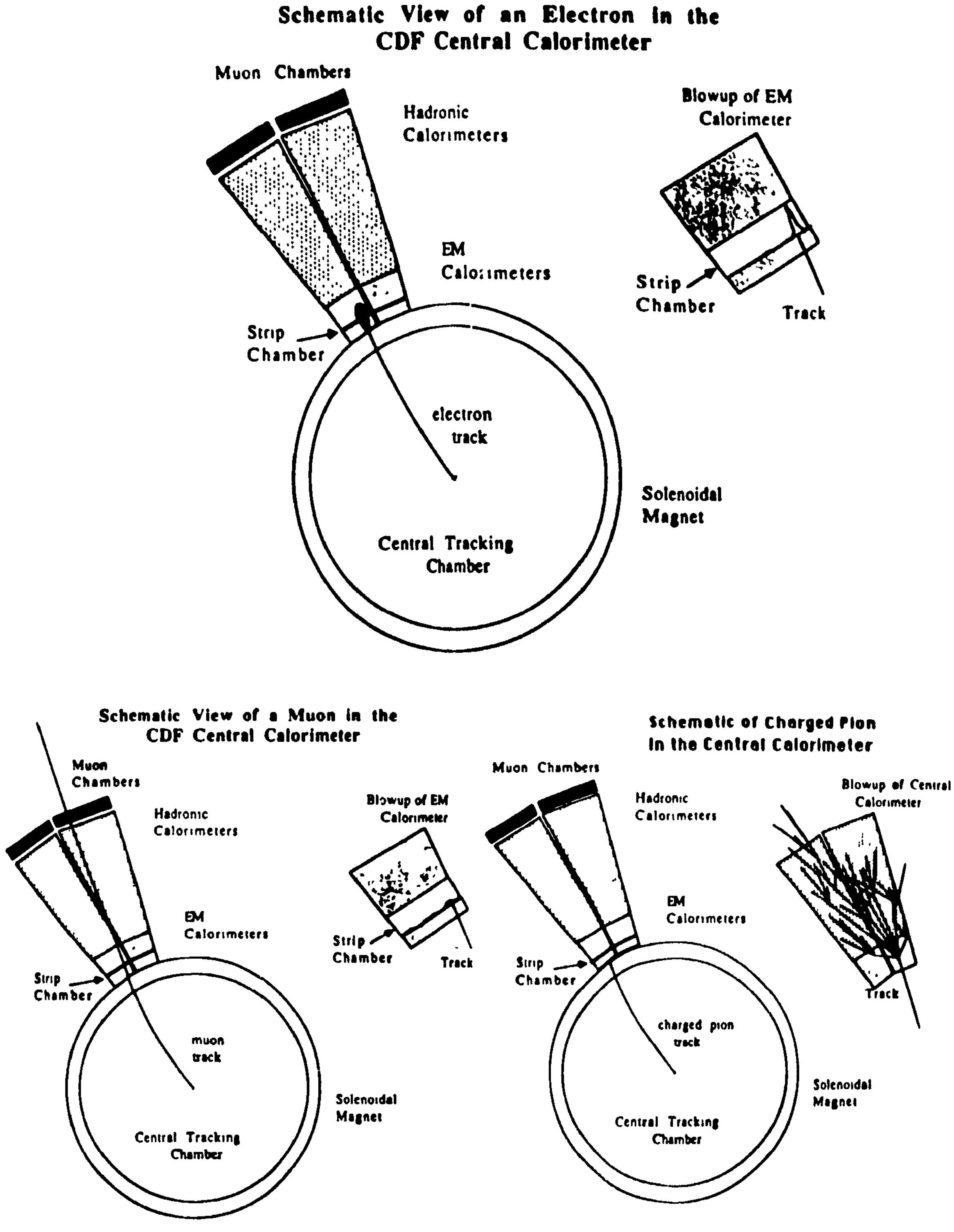

Figure 2.5: Schematic views of an electron, a muon and a charged pion in the CDF central calorimeter.

Chapter 3

Test Beam for CDF Central Calorimeter Modules

3.1 Test beams as a calibration tool

As we said in the previous chapter, the CEM and CHA modules (wedges) are instrumented with a pair of phototubes for each tower. These phototubes read the signal caused by the shower developed in the calorimeter. By knowing the signals of the phototubes, we can deduce the energy of the particle that entered the calorimeter.

In physics runs the front-end electronic scanners read out the charge integrating channels for the central calorimeter. For each channel the signal is digitized, then a pedestal is subtracted and the result (if it is above some digital threshold) is stored. When the time comes to use these values (to do physics analysis) we convert the stored values (counts) into energy (GeV) by multiplying them by the appropriate calibration constants which correct for channel-to-channel variations. The calibration constants and information relative to them are saved in a calibration data base.

In order to determine the calibration constants we need a number of calibration systems. The calibration systems used for the CDF central calorimeter are described in detail elsewhere [25]. Very briefly we can say that the response of the central calorimeter wedges was first measured with the use of a ^{60}Co source system that was later replaced by a ^{137}Cs source drive system (radioactive sources calibration). These two systems were used for primary calibration along with the response of the wedges to electrons and pions in a test beam. During physics runs the calibration obtained with the use of the above systems is supplemented by a fast calibration based on a LED flasher system and a Xenon flasher system, so as to carry on a daily calibration.

The importance of the test beam is not limited to the determination of the calibration constants only. The nominal response of electrons as concerns the lateral shower profiles in the CES and in the calorimeter was parametrized using 1985 test beam results (recall the χ^2 and L_{SHR} variables in section 2.3). The response maps for the central calorimeter towers (response vs. distance from tower center) and the parametrizations of the electromagnetic and hadronic showers are also obtained based on 1985 test beam results and are used for the simulation of the detector response (see eq. 2.2 for example).

3.2 The geometry of the CDF test beam

In order to study aspects of the central calorimeter response like the ones mentioned above, two extra central calorimeter modules (wedges) were constructed for CDF and were placed along the Meson Test (MT) beam line (see Fig. 3.1). The two wedges of the test beam are stacked together and they pivot about a point equivalent to the $z_{CDF} = 0$ interaction point at $B0$. Thus the wedges move in an arc and the test beam experiment is able to simulate the projective geometry of CDF. The way the wedges move allows scans in both η and ϕ directions. In front of the wedges there is an aluminum plate that simulates the number of radiation lengths a particle goes through while traveling from the interaction point to the face of the central calorimeter at CDF (i.e it simulates the beam pipe, the SVX, the VTX, the CTC, and the solenoidal coil). The aluminum plate moves with the wedges, and so the radiation lengths an incoming particle goes through change from tower to tower in exactly the same manner as happens in the CDF detector at B0. In the 1991 test beam the CPR (Central Preradiator) modules were located on the wedge in exactly the same manner as they are in CDF. The CPRs are strip chambers used to detect photons converted in the solenoidal coil ($\approx 0.85X_0$ thick) and are located on the wedges, just in front of the CEM towers.

As shown in Fig. 3.1, the MT beam line has several focusing and defocusing quadrupole magnets to guide the beam down the line, several targets that allow the production of beams in different momentum ranges, two sets of momentum selecting dipole magnets, a threshold Cerenkov counter to tag electrons (a synchrotron radiation counter, SRD, is also used to tag electrons), scintillation counters to monitor the beam intensity, proportional wire chambers (PWC) to monitor the beam profiles, a single wire drift chamber (SWDC) system to measure the trajectory and momentum of the particles directed onto the CDF test beam area, scintillators that are located

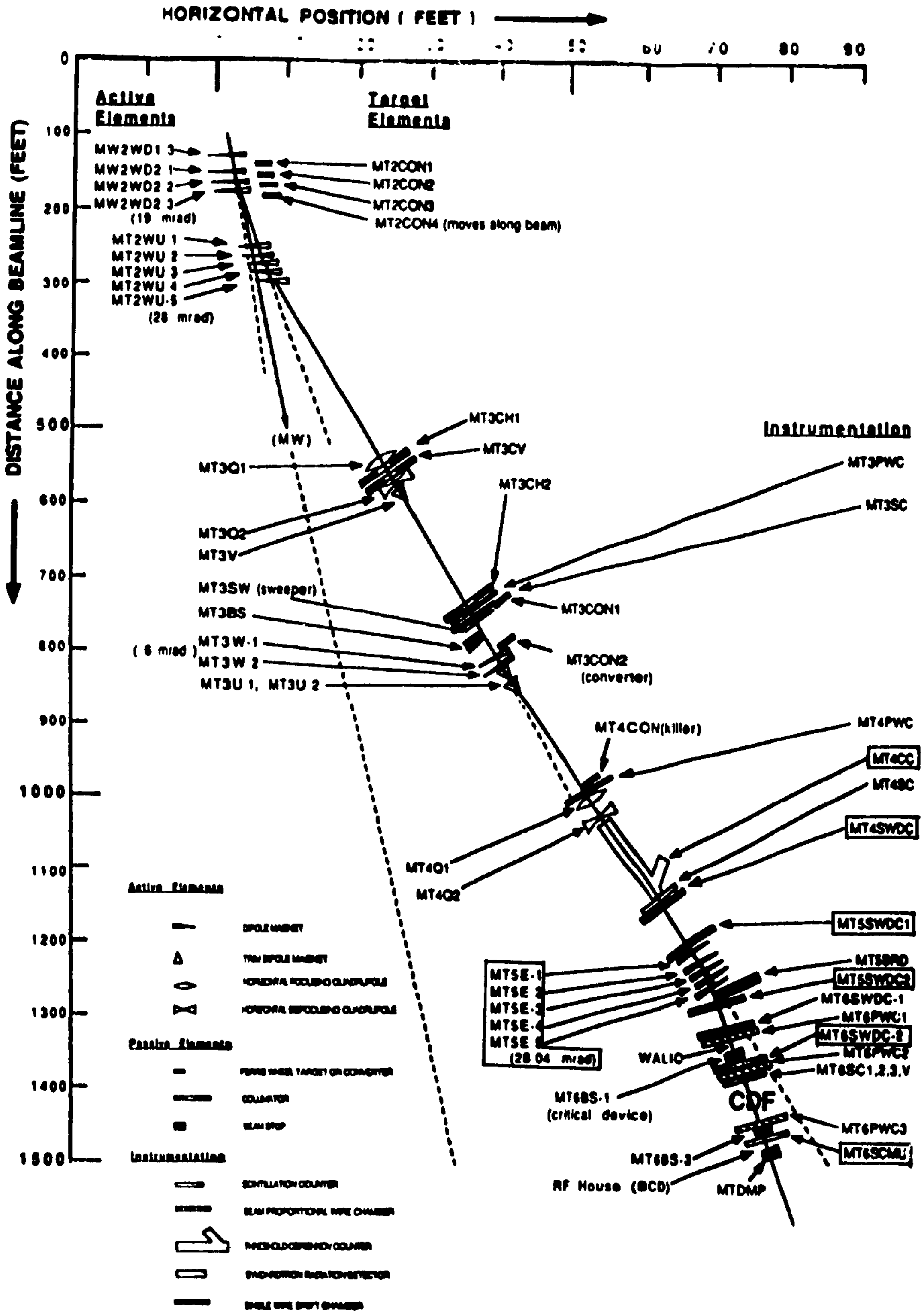

Figure 3.1: The Meson Test Beam line.

after the last SWDC and are used to trigger on an incoming charged beam particle, and two muon scintillators located behind the wedges (one just after them and one after ≈ 1 m of steel).

Of particular interest to us are the following instruments and elements: (a) The MT5E dipole magnet string which is the last before the beam reaches the wedges. It gives an approximate bend of 28 milliradians to the incoming beam. (b) The SWDCs used for the momentum measurement are MT4SWDC (located about 30 meters upstream of the bend string), MT5SWDC1 (located immediately before the bend string), MT5SWDC2 (located immediately after the bend string) and MT6SWDC-2 (located about 40 meters downstream of the bend string) [26]. (c) The scintillators located after the last SWDC (MT6SWDC-2), which are used to trigger an event. An event is discarded if it does not cause these scintillators to fire. The size and the location of the scintillators are such as to tell us that a particle which caused them to fire, will pass over the pivot point within a distance of ≈ 2.5 cm. (d) The Cerenkov threshold counter (MT4CC) which discriminates electrons from muons and pions up to momentum ≈ 25 GeV/c. (e) The scintillator MT6SCMU which is located behind the wedges and behind ≈ 1 m of steel, used to tag muons (for momenta above ≈ 25 GeV/c almost all the muons are able to reach this scintillator).

There are two coordinate systems used in the test beam: the local wedge system (see end of section 2.3 and Fig 2.2(a)), and the beam coordinate system which describes the position of the beam while traveling towards the wedges after the MT5E dipole magnet string. This is a modification of the "spectrometer coordinate system" used for the momentum determination of the beam particles [27]. We define the beam coordinate system with the horizontal z-axis to go through the centers of the last two SWDCs, the y-axis to be vertically upwards, and the x-axis to be orthogonal to the other axes making the system right-handed (see Fig. 3.2).

Each SWDC consists of four cells (see Fig. 3.2). Each cell is 2.54 cm thick and contains an anode wire sandwiched between two cathode planes. In each chamber two sense wires are horizontal (x-direction) and two are vertical (y-direction). Each pair is displaced symmetrically 20.3 mm from the SWDC center to resolve the right-left ambiguity. The vertical pair (used for the horizontal x-position measurement) is closer to the wedges. The horizontal pair (used for the vertical y-position measurement) is placed upstream.

In order to have an idea where a beam particle is going to hit the wedge, we use the position information obtained by the SWDCs, make the appropriate extrapolation

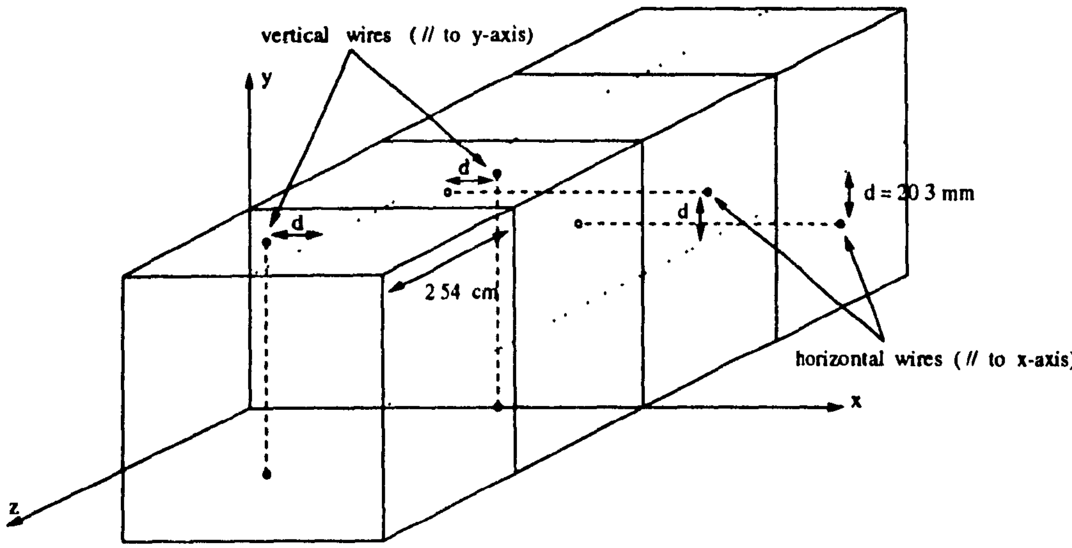

Figure 3.2: The last SWDC before the CDF test beam region (MT6SWDC-2 in Fig. 3.1). The beam coordinate system is also shown, having its origin on the face of this SWDC.

of the particle track to the face of the wedges and obtain the position where the incoming beam particle is expected to hit the wedge, in local wedge coordinates. This is important in order to form parameters like the Δx and Δz used for electron identification (see section 2.3).

The area of the CDF test beam wedges is shown in Fig. 3.3. Having this figure in mind, we note the following:

A point on the wedge with wedge coordinate z_{CES} (horizontal), has beam coordinates x' and z':

$$\begin{aligned} x' &= R_{CES} \cdot sin\theta_{Hsta} + (z_{CES} - z_{off}) \cdot cos\theta_{Hsta} \\ z' &= z_{pp} + R_{CES} \cdot cos\theta_{Hsta} - (z_{CES} - z_{off}) \cdot sin\theta_{Hsta} \end{aligned} \tag{3.1}$$

In order for this point to be on the particle trajectory, we must also have:

$$x' = x_0 + (z' - z_0) \cdot tan\theta_H, \quad \text{and therefore,}$$

$$z_{CES} = z_{off} + \frac{x_0 + (z_{pp} - z_0 + R_{CES} \cdot cos\theta_{Hsta}) \cdot tan\theta_H - R_{CES} \cdot sin\theta_{Hsta}}{cos\theta_{Hsta}(1 + tan\theta_{Hsta} \cdot tan\theta_H)} \tag{3.2}$$

A point on the wedge with wedge coordinate x_{CES} (vertical), has beam coordinates y' and z':

$$\begin{aligned} y' &= -R_{CES} \cdot sin\theta'_{Vsta} - x_{CES} \cdot cos\theta'_{Vsta} \\ z' &= z_{pp} + R_{CES} \cdot cos\theta'_{Vsta} - x_{CES} \cdot sin\theta'_{Vsta} \end{aligned} \tag{3.3}$$

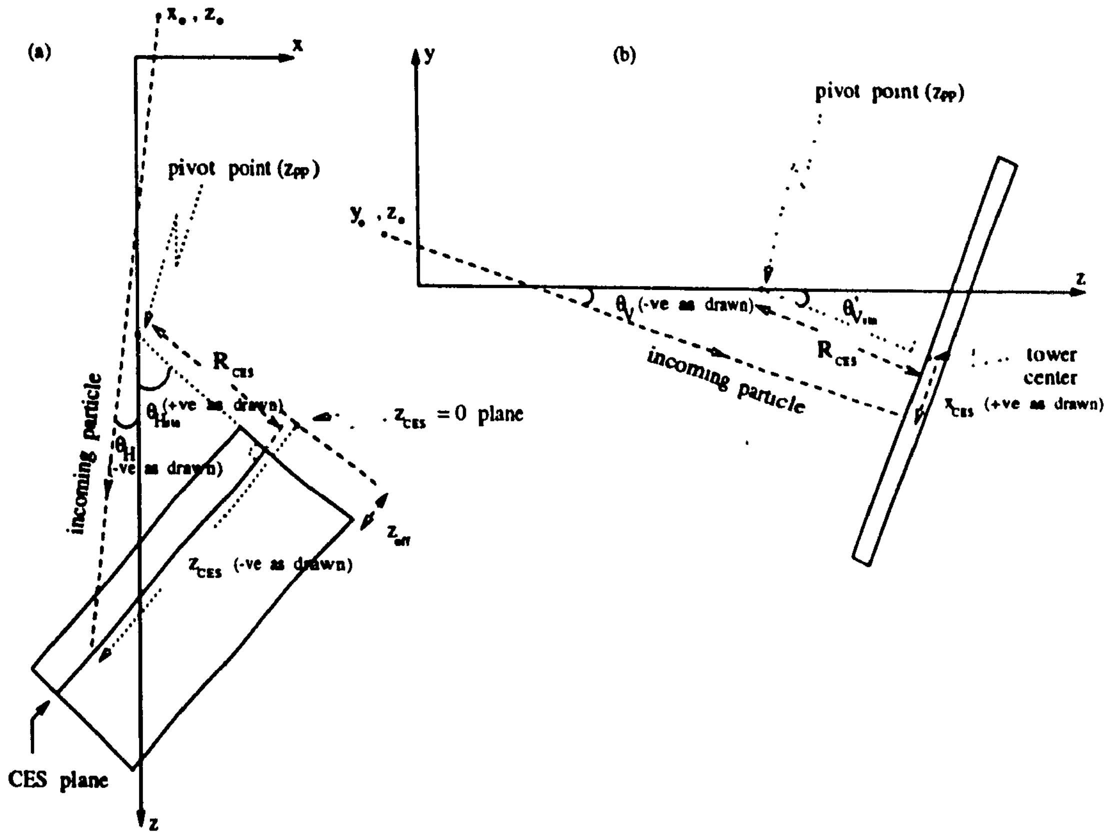

Figure 3.3: The CDF test beam region. (a) For wedge moving horizontally (x), and (b) for wedge moving vertically (y).

In order for this point to be on the particle trajectory, we must also have:

$$y' = y_0 + (z' - z_0) \cdot tan\theta_V, \quad \text{and therefore,}$$

$$x_{CES} = \frac{y_0 + (z_{pp} - z_0 + R_{CES} \cdot cos\theta'_{V_{sta}}) \cdot tan\theta_V + R_{CES} \cdot sin\theta'_{V_{sta}}}{cos\theta'_{V_{sta}}(-1 + tan\theta'_{V_{sta}} \cdot tan\theta_V)} \tag{3.4}$$

where:

(a) $\theta_{H_{sta}}$ is the horizontal stand position of the wedges ($\theta_{H_{sta}} = 0$ when an incoming particle with the nominal bend of 28.04 mrad is directed towards the tower 0 edge of the wedge), and $\theta_{V_{sta}}$ is the vertical stand position of the wedges, with $\theta'_{V_{sta}} = \theta_{V_{sta}} \pm 7.5°$ ($-$ for the lower wedge and $+$ for the upper wedge, because $\theta_{V_{sta}} = 0$ corresponds to the middle of the gap between the two wedges). Note here that, by definition, the horizontal position of the CES signal is negative, as if the wedges were in the $z < 0$ side in the CDF detector,

(b) θ_H and θ_V are the horizontal and vertical angles respectively, that the incoming particle forms with the line going through the centers of the last two SWDCs

(MT6SWDC2 and MT5SWDC2),

(c) x_0 and y_0 are the horizontal and the vertical positions of the incoming particle as they are measured at the last SWDC (MT6SWDC2),

(d) R_{CES} is the distance between the pivot point and the CES plane inside the wedges (R_{CES} = 184.15 cm),

(e) z_{off} is the distance between the $\theta = 90°$ plane at CDF and the highest θ edge of tower 0 (z_{off} = 4.22 cm as seen in table 2.1), and

(f) $z_{pp} - z_0$ is the distance between the pivot point and the MT6SWDC2 wire position that measures the horizontal (x_0) or the vertical (y_0) coordinate. For the horizontal measurement: $z_{pp} - z_0 = (329.83 + 3.81)$ cm, and for the vertical measurement: $z_{pp} - z_0 = (329.83 + 3.81 + 5.08)$ cm, where 329.83 cm is the distance between the pivot point and the face of MT6SWDC2 and the numbers 3.81 cm (= 1.5 in) and 5.08 cm (= 2 in) are related to the way the wires are placed inside the SWDCs (see Fig. 3.2).

Chapter 4

Elements of the CDF Monte Carlo

4.1 The CDF Monte Carlo

It is very useful for the understanding of the behaviour of the detector to have a software package that simulates the processes involved while particles are traveling through the detector material and the response of the detector components to these processes. Because many of these processes are of a statistical nature, the techniques used unavoidably make use of random numbers and are thus called Monte Carlo techniques.

There are two types of Monte Carlo packages at CDF: (a) The event generators, like ISAJET, PYTHIA and HERWIG, needed to simulate the processes involved from the proton-antiproton collision to the creation of the event particles, and (b) the detector simulators, namely QFL and CDFSIM, that simulate the CDF detector and its response to the particles created by an event generator. QFL uses parametrized responses rather than a first principle approach; CDFSIM is closer to a first principle approach, with the exception of the handling of showers in the calorimeters where the energy deposition is done by using equations that involve parameters determined at 1985 test beam studies, and is thus more time consuming (e.g. see eq. 2.2).

We are interested in investigating CDFSIM performance by doing a comparison between Monte Carlo and 1991 test beam data and we thus concentrate on describing the CDFSIM approach to the CDF detector simulation. Note also here that much of the parametrization for the simulation has been done with 1985 test beam results, and so the comparison between recent (1991) test beam data and the simulation is not redundant.

The procedure for simulating an event at CDF is as follows [28]:

(a) A list of the particles produced at the primary event vertex (using one of the

event generators) is read in.
(b) Each particle, one at a time, is traced through the simulated detector regions. Each region has its own characteristics (material type, shape and extent in space, the type of data it generates, locations of various read-out channels, etc.). As the particle traverses each detector region, it undergoes multiple Coulomb scattering, dE/dx energy loss, decays, hadronic interactions, etc. and as it travels through sensitive detector regions (i.e tracking detectors or calorimeters) it generates information (hits on wires / silicon wafers, or energy deposition). The particle is traced until it stops by decaying, converting, showering in the calorimeter, or exiting the detector region. If a particle decays, the decay products are added to the particle list and are treated as every other particle.
(c) After all the particles have been treated in this way, the "data" that each particle created are reformed into detector-oriented banks as if they had been real CDF data.

4.2 Energy deposition and related variables

Every particle that is taken out of the particle list in order to be stepped through the detector, is assigned a number of radiation lengths (if it is a γ or $e^{\pm}$) or a number of interaction lengths (if it is a hadron), at which the particle will interact (convert or shower). The particle is also assigned a path length in cm before it will decay (if this is desired and allowed). These numbers are extracted from exponential probability distributions.

Next the particle is stepped through the different detector elements. After each step, the number of radiation/interaction lengths the particle has traversed so far is calculated, and the number of radiation/interaction lengths left until it will interact is updated.

If the particle is ionizing, it suffers dE/dx in each of these steps. If the current detector is a calorimeter, then the energy lost (dE) is deposited in the tower the particle hit (for energy deposition in calorimeters, see below). This process of stepping, dE/dx and energy deposition continues until the particle either: (i) has kinetic energy less than 10 MeV and so deposits it all and ceases to exist, (ii) showers (see next paragraph), (iii) decays, or (iv) leaves the CDF volume.

Depending on the particle type the shower is considered to be electromagnetic or hadronic. In order to make the simulation of showers fast, the centroid of the shower is considered as a neutral particle traveling in the same direction as the particle immediately before showering. This neutral particle is now stepped through the different detector regions exactly as if it was a regular particle. The number of radiation and interaction lengths traversed since showering are updated after each step and the shower development is parametrized in terms of these two quantities.

The energy deposited within each step is calculated according to the longitudinal shower development formulas given in [18], where the parameters are determined through comparison with 1985 test beam data (see for example eq. 2.2 and [19]). The energy lost is stored in two parts: electromagnetic and hadronic energy loss (electromagnetic showers have no hadronic energy component, whereas hadronic showers have an electromagnetic component too).

The hadron shower simulation treats the shower as the sum of two components: a "charged π" shower with a scale of interaction lengths (hadronic component), and a "π^o" shower with a scale of radiation lengths (electromagnetic component). The electromagnetic fraction of hadronic showers is determined by using 1985 test beam data ([19], [29]). The electromagnetic contribution to a shower is 100 % for electromagnetic showers and 40 % for hadronic showers. The response of the calorimeter to the hadronic part of a shower is 40 % of its response to the electromagnetic showers [29].

If the current detector is a calorimeter, then the energy lost by the shower is deposited in the hit tower and the 8 (or 24, depending on the transverse shower size in comparison with the calorimeter tower size) neighbouring calorimeter towers. If the particle is a minimum ionizing particle, the energy is deposited in the hit tower only. The lateral shower development, as a function of the g/cm^2 of material traversed since the shower started, is calculated at every step[1]. The energy deposited is used to calculate an equivalent number of minimum ionizing particles (N), and $\sqrt{N}$ fluctuations to that number give statistical fluctuations to the energy deposited in the calorimeter.

The energy sharing between the neighbouring towers is done by integrating the transverse shower profile at the current depth over the areas of the 9 or 25 calorimeter towers, to find the fractions of deposited energy that go into each tower (note that the sum of the fractions is not usually one, due to losses in cracks or dead detector areas). A gaussian lateral energy distribution for electromagnetic showers, and an exponential distribution for hadronic showers is assumed.

[1]The parameterization follows the work of Abshire et al , Nucl Instrum Methods A **164** 67-77, with some simplifying assumptions

The energy deposited in a tower is then split between the two phototubes, in the central calorimeter. A two component exponential splitting function, with attenuation lengths of 100 cm (long) and 15 cm (short), is used for the CEM detector. 85 % of the energy is assumed to be attenuated with the long component. For the CHA detector a single component exponential with a 100 cm attenuation length is used to split the energy between the two phototubes. The energy is assumed to be deposited at the location of the shower centroid (or the position of the particle if it is minimum ionizing). The phototube pulse heights are independently fluctuated to produce a position resolution of 4 cm, for the CEM, or 5 cm for the CHA.

The process of stepping, energy loss, energy sharing and depositing in the calorimeters continues until the particle runs out of energy (less than 10 MeV), or exits the calorimeter.

By having simulated the energy deposition of the particle we can calculate quantities like E_{CHA}/E_{CEM} and L_{SHR} described in section 3.3.

4.3 The CES χ^2

As already said, every central calorimeter wedge has a strip chamber (CES) embedded in its electromagnetic compartment, at a depth of $\approx 5X_0$ ($\approx 6X_0$, including the material between the interaction point and the front plate of the central calorimeter[2]).

4.3.1 The CES geometry

The strip chamber uses the "local" coordinate system of the wedge (see end of section 2.3 and Fig. 2.2(a)). Strips (the cathodes) and wires (the anodes) are placed perpendicular to each other in order to determine the z and x (or ϕ) position of the shower, respectively. In the case of a shower, its transverse spread is also determined through strip and wire information.

Strips are parallel to the local x-axis, with $6.0 \text{ cm} \leq |z_{CES}| \leq 239.4$ cm [3]. There are 128 strips per wedge, each of width ≈ 0.159 cm. The distance between the midpoints of two consecutive strips is $\approx$ 1.67 cm for strips in towers 0 to 4, and ≈ 2.01 cm for strips in towers 5 to 9. Wires are parallel to the z-axis. The spacing between the wires is ≈ 1.45 cm and is such that 32 of them cover the wedge in the ϕ direction (from $x_{CES} = -22.5$ cm to $+22.5$ cm). The CES is split in z into two

[2] About 85 % of this extra $1X_0$ is at the solenoid coil.

[3] The local x, y and z coordinates will be called x_{CES},y_{CES} and z_{CES} from here on

pieces ($6.0 < |z_{CES}| < 121$ cm and $121 < |z_{CES}| < 239.4$ cm), with 32 wires in each segment for a total of 64 wires per wedge.

Notice that the $\theta_{CDF} = 90°$ crack and the construction of the wedge modules do not allow coverage at smaller $|z|$.

4.3.2 Simulation of the CES response

Given the location of a particle or shower that traverses the strip chamber, a list of the strips/wires that may have energy deposition is obtained. In the case of a minimum ionizing particle, only 1 channel is assumed to be hit; for a shower, we assume 9 channels (or 18 if we look at the wire channels and the particle is close to the boundary of the two CES segments at $|z_{CES}| = 121$ cm).

Next the sigma of the lateral energy deposition for the particle is obtained. This sigma is small if the particle is minimum ionizing, and equal to the shower transverse sigma if we deal with a shower. Actually in the CDFSIM Monte Carlo the transverse development of the shower is parametrized as two gaussians; a "narrow" and a "wide" component, where the narrow component carries 60 % of the energy and has $\sigma_{narrow} = (0.62 \pm 0.09)$ cm, whereas the wide component has $\sigma_{wide} = 2.21$ cm [4].

The fractional energy sharing between the strips[5] is obtained by calculating the fraction of the energy that should be deposited on each strip. This is done by integrating the transverse profile of the shower over the surface covered by the 9 previously selected strips, by making use of the σ's of the transverse profile and the geometry of the strips.

For electromagnetic showers the response of the strip chambers is non-linear with respect to the incident energy (E_{inc}), and the energy response is a function of $sin\theta$[6]; the energy deposition (E_{dep}) is obtained by correcting the incident energy for these factors (these dependencies were determined from 1985 test beam data).

Next a resolution σ_E is assigned to this energy ($\sigma_E/E_{dep} = 0.17 + 0.50/E_{inc}$, where E_{inc} is in GeV). Fluctuations on the deposited energy are taken into account by extracting a new E_{dep} value, E'_{dep}, from a gaussian with a central value of E_{dep} and a sigma of σ_E. This deposited energy is shared among the strip channels by using

[4]Both these sigmas are given here for the shower at the depth of the CES

[5]In the rest of this section we use the word "strips" for convenience, but the analysis is the same for the wire channels.

[6]The shower goes through more material (and so it contains more particles at shower maximum) and the shower particles travel a longer path in the CES chamber and cause more ionization, when they travel at higher $|z|$ values (see Fig 4 1)

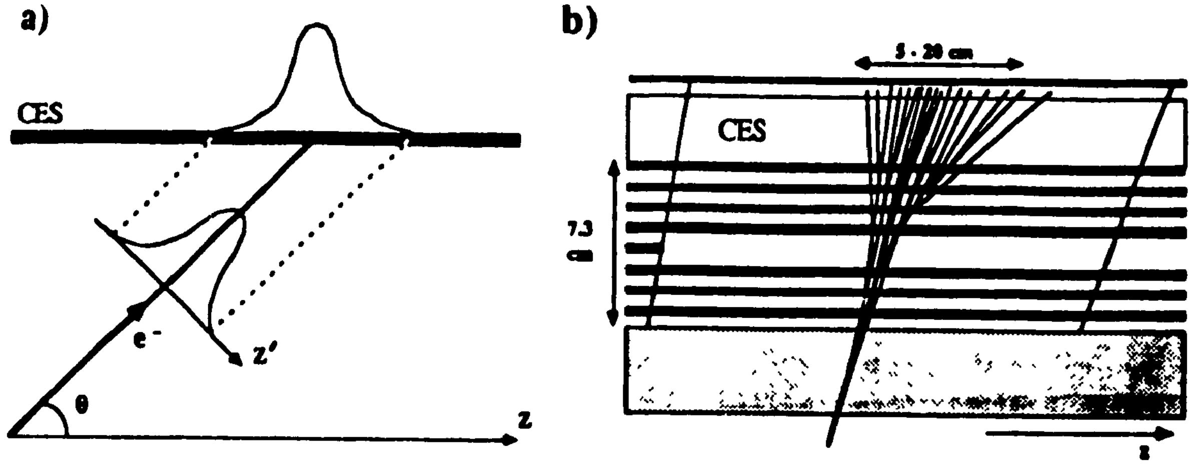

Figure 4.1: a) The $1/\sin\theta$ widening of showers in the strip view. b) The origin of the asymmetry in the strip profile is schematically illustrated.

the sharing fractions calculated previously (so $E_i = f_i * E'_{dep}$, where E_i and f_i are the energy and the sharing fraction corresponding to the i^{th} strip).

The effective number of minimum ionizing particle equivalents (MIPEs) for each strip is calculated next ($N_i = E_i/E_{MIPE}$ for the i^{th} channel, with E_{MIPE} to be 0.156 GeV from Monte Carlo calculations done for 50 GeV incident electrons). Channel fluctuations, in order to simulate the shape fluctuation of the shower, are calculated by extracting a new N_i, N'_i, from a gaussian with sigma equal to $\sqrt{N_i}$. The energy for each strip channel is then modified so as to be $E'_i = N'_i * E_{MIPE}$. The total deposited energy is calculated again by using the new E'_i values ($E_{total} = \sum_i E'_i$), and is then normalized to the E'_{dep} value previously calculated so as to give a normalization factor ($F_{norm} = E_{dep}/E'_{total}$). F_{norm} is then used to modify once again the energy deposited on each strip ($E''_i = E'_i * F_{norm}$).

Because the test beam data show that the responses of the strips and the wires agree at the $5-10$ % level, the strip responses are renormalized to the wire responses with a 90 % correlation and the strip energy is corrected for this factor. Thus we have for the strips: $E^{final}_{i,strips} = E''_{i,strips} * (\sum_i E''_{i,wires} / \sum_i E''_{i,strips}) * F_{correl}$, where F_{correl} is a factor extracted from a gaussian with central value 1.0 and sigma equal to 0.1. The energy deposited on the i^{th} wire is $E^{final}_{i,wires} = E''_{i,wires}$.

Finally the energies deposited to each strip channel are converted into ADC counts, by using a gain of 700 ADC counts per GeV of deposited energy, and the results are stored into "banks" with the same structure as the real data banks.

4.3.3 The definition of the CES χ^2

The CES χ^2 is a pseudo-χ^2 used to evaluate the agreement between a given CES cluster and a standard electromagnetic shower transverse profile obtained with the help of 1985 50 GeV/c test beam electron data.

Given a CES cluster, a standard electromagnetic shower transverse profile is produced: At first the central shower position (x_0) is found, by starting with the position of the highest energy channel and fitting the measured energies of the CES channels to the energies expected to appear on these channels, according to 1985 test beam electron data. After the central position of the shower is found, the profiles for transverse deposition of energy obtained from 1985 test beam electron data are used to calculate a "standard" transverse profile for a CES shower with central position x_0 [22]. Note that the shape of the 1985 test beam profiles was found to be independent of the electron energy. The standard profiles provide us with the fractional energy deposited in a channel a distance x from the shower center.

Then the CES χ^2 in either the strip or the wire view, is given by [22]:

$$\chi^2 = \frac{1}{4} \sum_{i=1}^{7or11} \frac{[y_i - y(x_i)]^2}{\sigma_i^2} \tag{4.1}$$

where i is the CES strip or wire channel index and we can use 7 or 11 channels for the comparison, y_i is the measured profile normalized to unity, $y(x_i)$ is the standard normalized 1985 test beam electron profile obtained from the fitted central shower position, and σ_i^2 is the estimated variance for the i^{th} channel of the standard profile:

$$\sigma_i^2 = \sigma_{10,i}^2 (\frac{10}{E})^{0.747} \tag{4.2}$$

where

$$\sigma_{10,i}^2 = (0.096)^2 y(x_i) + (0.026)^2 \tag{4.3}$$

is the variance of channel i in the normalized profile determined from 10 GeV/c test beam (1985) electrons. The scaling with energy for σ_i^2 was determined from the measured CES response vs. energy in 1985 test beam data.

A small CES χ^2 therefore indicates that the current CES cluster has a shape consistent with the shape expected from incoming $e^{\pm}/\gamma$. Cuts on the CES χ^2 are widely used to select electrons in our data samples (see section 2.3).

Chapter 5

Comparison of Test Beam and Monte Carlo Electron Response

5.1 Test beam electron data

The electron samples used in this analysis come from files of about 1000 particles shot towards the center of the lower wedge towers; mostly tower 4 data were used. The incoming beam is not a "pure" one; it is a mixture of electrons, pions and muons. When the incoming beam is an "electron" beam, we know that most, but not all, of the beam particles are electrons. Thus we have to find a way to reject the incoming muons and pions in order to compare the response of the calorimeter to test beam electrons with its response to simulated electrons. The cuts used to select the electron samples are:

(a) A cut to reject minimum ionizing particles (muons and punch through pions) as well as some of the showering pions:

$$E_{CEM} \quad > \quad 0.6 \quad P_{inc} \tag{5.1}$$

where E_{CEM} is the energy in the 3 η-adjacent CEM towers that contain the electromagnetic shower and P_{inc} is the momentum of the incoming particle. This is a strict cut for muon rejection, since muons are minimum ionizing particles and the probability to deposit a relatively large amount of energy (due to Landau fluctuations) in the CEM is very small; most of the muons deposit less than 1.5 GeV in the CEM. We can predict the response of the central calorimeter to muons, by calculating their energy loss based on Landau's theory. The calculated energy loss of muons of two different energies, in the central calorimeter, is shown in Fig. 5.1. In table 5.1, the percentage of muons that survive the $E_{CEM} \; > \; 0.6 \; P_{inc}$ cut, is shown.

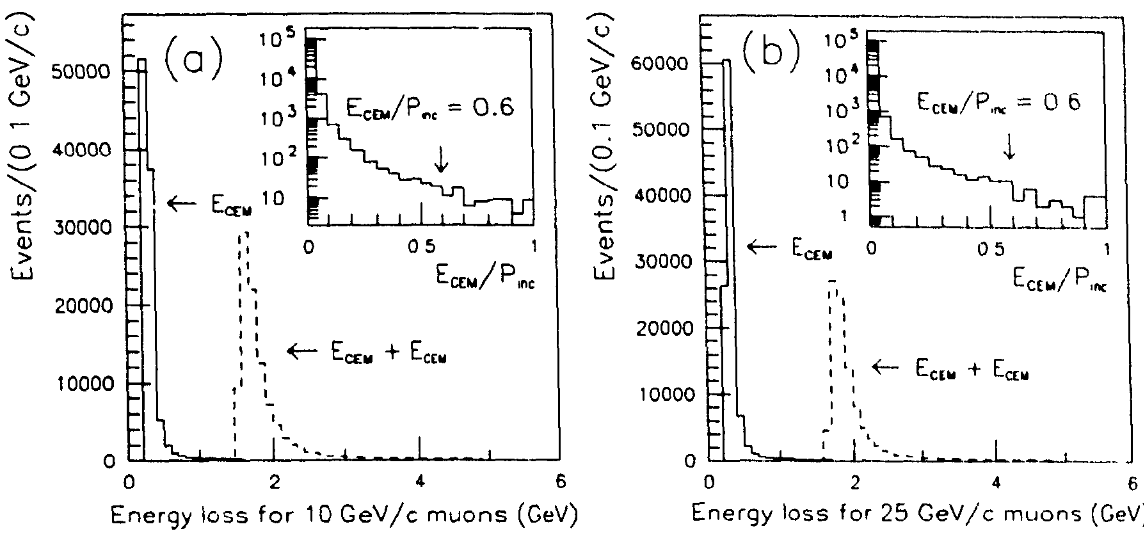

Figure 5.1: Muon energy loss in the central calorimeter (center of tower 4) and E_{CEM}/P_{inc} distributions for 10 GeV/c (a) and for 25 GeV/c (b) muons (based on Landau's theory).

By keeping events with $E_{CEM} > 0.6\ P_{inc}$ we also reject punch-through as well as showering pions. We know that electrons should deposit almost all of their energy in the electromagnetic part of the calorimeter; pions deposit energy primarily in the hadronic part of the calorimeter. Thus, by keeping events with a significant amount of energy in the CEM we reject most of the pions, but since the CHA is behind the CEM, it is always possible to have some pions that "pre-shower" and so deposit a significant amount of energy in the electromagnetic part of the calorimeter. In table 5.2, the percentage of pions that survive the $E_{CEM} > 0.6\ P_{inc}$ cut, is shown.

In order to make the rejection of muons more reliable, we could have used the scintillator MT6SCMU which is placed behind the wedges with ≈ 1 m of steel between the wedges and the scintillator (a particle must traverse ≈ 10 interaction lengths of material to reach this scintillator). But since the above cut is so efficient on removing the muons, we do not use it. In order to select electrons we could have also used the Cerenkov counter information. For particles up to ≈ 25 GeV/c, the difference in the responses due to electrons and muons or pions is quite clear; only electrons travel faster than the speed of light in the gas of the Cerenkov counter. As the beam energy increases the Cerenkov becomes sensitive to muons and pions and so at 50 GeV/c the Cerenkov counter is already useless. Note nevertheless that since the Cerenkov information can be applied with some degree of confidence only in the 10 GeV/c and

Initial momentum, P_{inc} (GeV/c)	% of muons surviving the $E_{CEM} > 0.6P_{inc}$ cut
10	0.0768 ± 0.0028
25	0.0326 ± 0.0018
50	0.0131 ± 0.0012
100	0.0062 ± 0.0008

Table 5.1: Percentage of muons surviving the $E_{CEM} > 0.6P_{inc}$ cut (calculated using the Bethe-Bloch formula and Landau's theory for the energy loss).

Initial momentum, P_{inc} (GeV/c)	% of pions surviving the $E_{CEM} > 0.6P_{inc}$ cut
9.76 ± 0.22	3.98 ± 0.12
26.18 ± 0.33	4.05 ± 0.12
48.21 ± 0.78	4.65 ± 0.12
101.3 ± 2.6	4.42 ± 0.12

Table 5.2: Percentage of pions surviving the $E_{CEM} > 0.6P_{inc}$ cut (calculated with the CDF simulation, see sections 4.1 and 4.2).

25 GeV/c particles, but not for higher momentum, we choose not to use the Cerenkov information, but rather use uniform selection criteria for all the data samples. Notice that the single cut already applied is quite efficient for our analysis.

(b) A cut to prevent events with more than one in-time particle (i.e events with substantially more energy than the momentum measurement indicates we should expect):

$$E_{CEM} + E_{CHA} < 1.3 \quad P_{inc} \tag{5.2}$$

Events with $E_{CEM} + E_{CHA} < 1.3 \quad P_{inc}$ occur at the < 1 % level.

(c) Spurious signals coming from a "hot" strip channel in the CES chambers that fired frequently in the absence of a particle, are excluded by rejecting signals with:

$$-72 \quad \text{cm} < z_{CES} < -71.8 \quad \text{cm} \tag{5.3}$$

Events with no information on the momentum measurement (P_{inc}) or the stand position ($\theta_{H_{sta}}$ and $\theta_{V_{sta}}$) of the test beam wedges are also rejected, since this information is either used in other cuts, or it is essential to calculate some of the variables to be compared.

Momentum (GeV/c)	f_π^{in}	f_e^{in}	$N_{all}^{in,TB}$	$N_{all}^{in+out,TB}$	f_π^{TB}
9.76 ± 0.22	0.252 ± 0.013	0.986 ± 0.001	546	562	0.020 ± 0.010
26.18 ± 0.33	0.397 ± 0.014	0.966 ± 0.002	531	557	0.022 ± 0.016
48.21 ± 0.78	0.373 ± 0.013	0.930 ± 0.003	534	602	0.077 ± 0.031
101.3 ± 2.6	0.254 ± 0.012	0.820 ± 0.004	482	591	$< 0.0615 @ 90\% CL$

Table 5.3: Fraction of pions in the test beam samples after the cuts (f_π^{TB}).

(d) And, finally, a cut to keep electrons in a specific x_{CES} and z_{CES} region so as to have an electron sample with a uniform or linear distribution of the incident particle positions, as these are measured at the SWDCs and extrapolated to the face of the CES. This cut is applied in order to simplify the generation of Monte Carlo samples that look like the test beam electron samples.

Having selected our data samples by applying the cuts mentioned above, we can calculate the percentage of pions that are left in our final samples assuming that the muon contamination is negligible (see table 5.1). Let N_e^{TB} and N_π^{TB} be the number of electrons and pions respectively in our final test beam sample, and f_e^{in} and f_π^{in} be the fraction of electrons and pions respectively that have $E_{CHA}/E_{CEM} < 0.055$, where E_{CHA} is the energy in the 3 CHA towers behind the 3 CEM towers that contain the electromagnetic shower. We choose that value as the boundary for the "in" and "out" regions, so as to have reasonable "in" and "out" samples in our test beam data.

We can determine N_e^{TB} and N_π^{TB} by solving the two equations:

$$f_e^{in} N_e^{TB} + f_\pi^{in} N_\pi^{TB} = N_{all}^{in,TB} \qquad (5.4)$$

$$N_e^{TB} + N_\pi^{TB} = N_{all}^{in,TB} + N_{all}^{out,TB} \qquad (5.5)$$

where $N_{all}^{in,TB}$ ($N_{all}^{out,TB}$) is obtained by counting the number of events that lie below (above) $E_{CHA}/E_{CEM} = 0.055$ in the test beam sample in question after all the cuts are applied.

Then the fraction of pions in our test beam data sample, f_π^{TB}, will be:

$$f_\pi^{TB} = \frac{N_\pi^{TB}}{N_{all}^{in,TB} + N_{all}^{out,TB}} = \frac{1}{f_e^{in} - f_\pi^{in}} \cdot \left(f_e^{in} - \frac{N_{all}^{in,TB}}{N_{all}^{in,TB} + N_{all}^{out,TB}}\right) \qquad (5.6)$$

where f_e^{in} and f_π^{in} are calculated from Monte Carlo pure electron and pion samples independently after the application of cuts (a) and (b). The results of such calculations for data samples of approximately 10, 25, 50 and 100 GeV/c electrons shot towards the center of tower 4 are given in table 5.3.

5.2 Monte Carlo reproduction of test beam data

We used a single particle event generator to generate the electron samples, and the CDFSIM full detector simulation[1] to simulate the detector and its response to the single particles traversing the central calorimeter.

For every test beam file with particles in a certain momentum region directed towards a specific tower, an electron Monte Carlo sample is generated with the same spread in momentum and incident CES positions. The momentum of the generated particles is spread as a gaussian with width and central values determined from these test beam data.

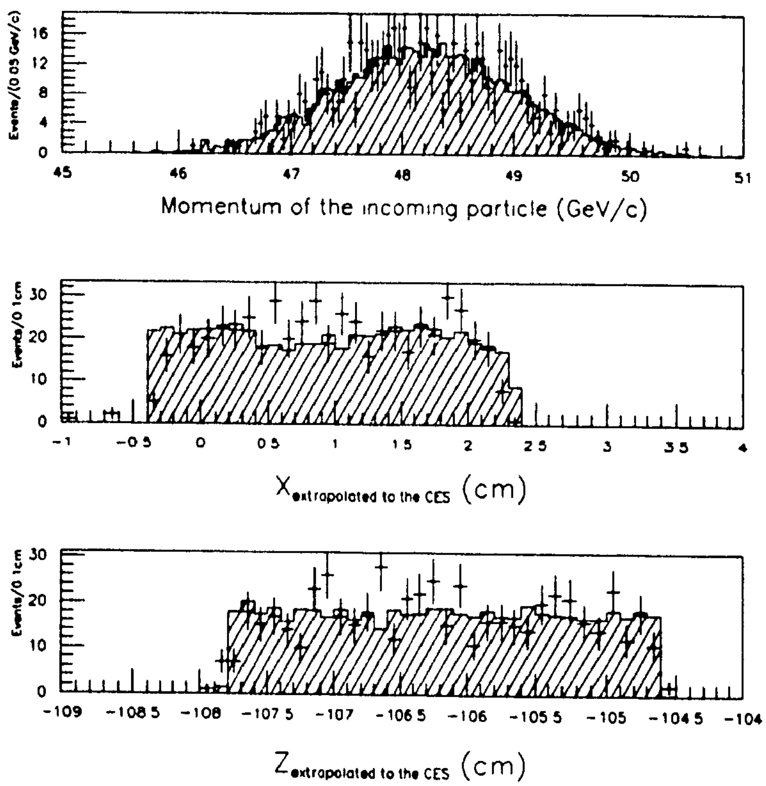

Figure 5.2: Momentum and extrapolated hit position for test beam and Monte Carlo electrons. Test beam (points with error bars) and Monte Carlo (histograms) electrons with momentum ≈ 48 GeV/c shot towards approximately the center of tower 4 are used for these figures.

Fig. 5.2 shows the momentum and the spread of the incident CES positions for a test beam file of electrons with momentum ≈ 48 GeV/c shot towards approximately

[1]CDFSIM is described in chapter 4 (sections 4.1 and 4.2).

Inset in Fig. 5.3 - 5.8	P_{inc} (GeV/c)	z_{CES} (cm)	x_{CES} (cm)	tower #
(a)	9.76 ± 0.22	-108.3 to -104.6	-0.08 to 2.9	4 center
(b)	26.18 ± 0.33	-107.9 to -104.5	-0.2 to 2.5	4 center
(c)	48.21 ± 0.78	-107.8 to -104.6	-0.4 to 2.4	4 center
(d)	53.69 ± 0.78	-36.1 to -33.4	-0.6 to 1.8	1 center
(e)	53.72 ± 0.78	-108.0 to -104.7	-0.4 to 2.0	4 center
(f)	48.26 ± 0.79	-156.6 to -152.1	-0.2 to 2.5	6 center
(g)	100.9 ± 2.6	-97.2 to -93.7	0.2 to 2.6	3 and 4
(h)	100.9 ± 2.9	-102.2 to -99.0	0.2 to 2.4	4 close to 3
(i)	101.3 ± 2.6	-111.7 to -105.5	0.2 to 2.1	4 center

Table 5.4: Momentum, z_{CES} and x_{CES} for the test beam files used in Fig. 5.3 to 5.8.

the center of tower 4, and the same quantities for the corresponding Monte Carlo sample.

5.3 Test beam vs Monte Carlo comparison on the basis of 6 variables

As explained in section 2.3, electrons in CDF can be identified by using a number of designated variables. Six of these variables are used to test the quality of the CDF central calorimeter simulation[2]: E_{CHA}/E_{CEM}, L_{SHR}, Δz, Δx, χ^2_z and χ^2_ϕ [3].

Electrons of approximately 10, 25 and 50 GeV/c shot towards approximately the center of tower 4 (see table 2.1 and rows (a), (b) and (c) in table 5.4 for the coordinates[4]), are used for the test beam vs Monte Carlo comparison of the above mentioned variables (see insets (a), (b) and (c) in Fig. 5.3 - 5.8).

Next we compare the same variables for $\approx$ 50 GeV/c electrons shot towards approximately the centers of towers 1, 4 and 6 (see table 2.1 and rows (d), (e) and (f) in table 5.4 for the coordinates). The comparison is demonstrated in insets (d), (e) and (f) in Fig. 5.3 - 5.8.

Lastly we compare the same variables for $\approx$ 100 GeV electrons shot towards

[2]Note that here we choose to use basically only one cut ($E_{CEM} > 0.6 P_{inc}$), so as to proceed in a bias-free comparison between the test beam and the Monte Carlo

[3]For the definition of the χ^2s see section 4.3.3. For a definition of the other variables see section 2.3

[4]The z coordinates are negative for the test beam data, since the test beam wedges are defined to be "$z < 0$" wedges.

different z regions of tower 4 (see table 2.1 and rows (g), (h) and (i) in table 5.4 for the coordinates). The comparison is demonstrated in insets (g), (h) and (i) in Fig. 5.3 - 5.8.

We observe the following from Figures 5.3 - 5.8:

• E_{CHA}/E_{CEM} is in good agreement between the test beam and the Monte Carlo. We observe that the E_{CHA}/E_{CEM} distributions shift towards higher values as the energy increases for both test beam and Monte Carlo electrons (see Fig. 5.3 (a), (b), (c) and (i)); this is due to the fact that the longitudinal dimension of the showers increases as the energy of the incoming particle increases (see eq. 2.2). The E_{CHA}/E_{CEM} decreases as the tower number increases since the electron has to go through some extra material to reach the CHA face (see Fig. 5.3 (d), (e) and (f)), whereas it increases slightly as we approach the center of the tower (see Fig. 5.3 (g), (h) and (i)).

• L_{SHR} for Monte Carlo events is always more negative than the L_{SHR} for test beam electrons. This is due to the fact that there is very little or no energy deposition in the neighbouring towers for the Monte Carlo electrons if they were shot towards the center of the towers. Recalling eq. 2.7 we can see that the absence of such energy deposition causes L_{SHR} to be always negative. This is not the case for the test beam electrons that deposit approximately 1 % of their energy in the neighbouring towers. This discrepancy may indicate that the showers in the simulation are not wide enough. Note also that L_{SHR} is narrower for the Monte Carlo electrons shot towards the tower centers. This is also due to the absence of substantial energy deposition in adjacent towers in the Monte Carlo; this in turn leads to a narrower L_{SHR} distribution, because only fluctuations of the expected energy give rise to the L_{SHR} width (see eq. 2.7).

From Fig. 5.4 (d), (e) and (f) we see that the L_{SHR} distribution becomes wider as the tower number increases for Monte Carlo events, which is due to the presence of some energy in the neighbouring towers as the seed tower number increases, because the cross sections of the towers decrease since the towers have the same η size.

From Fig. 5.4 (g), (h) and (i) we see that the L_{SHR} distribution for Monte Carlo events moves closer to the test beam values as the electrons approach the edges of the tower[5]. This shift is due to the fact that there is significant energy deposited in the neighbouring towers in this case, and it indicates that the shower width in the simulation is enough to deposit energy in the neighbouring towers only if the

[5]The L_{SHR} distribution for electrons in tower 4 but close to the tower 3 boundary (see Fig. 5.4 (h)), is wider for Monte Carlo, since a significant fraction of these events have not enough energy deposition to the neighbouring towers, and so the more negative peak appears too.

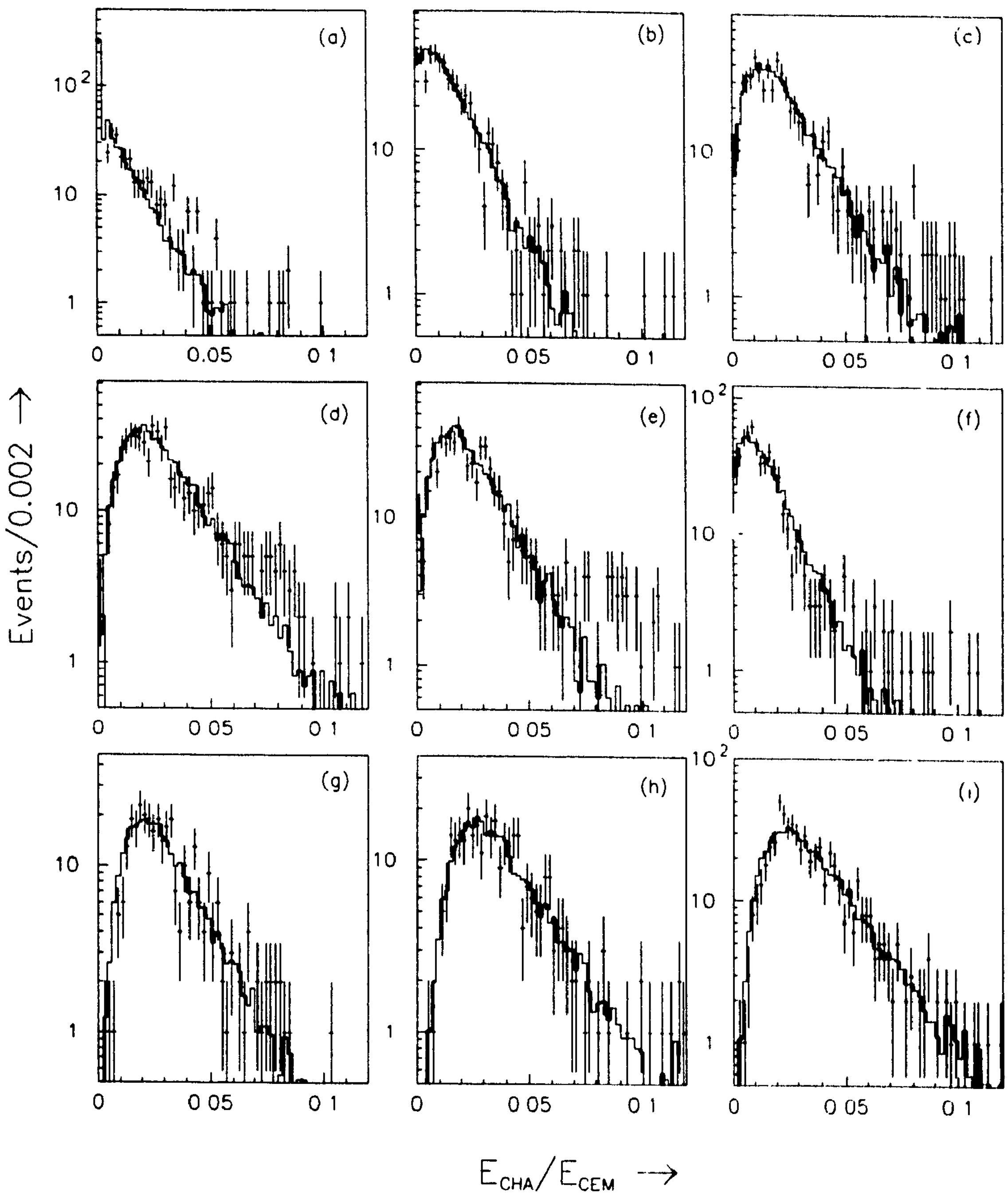

Figure 5.3: E_{CHA}/E_{CEM} for test beam (points with error bars) and Monte Carlo (histograms) events. (a), (b) and (c) for ≈ 10, ≈ 25, and ≈ 50 GeV/c electrons shot towards approximately the center of tower 4; (d), (e) and (f) for ≈ 50 GeV/c electrons shot towards approximately the centers of tower 1, 4 and 6 respectively; (g), (h) and (i) for ≈ 100 GeV/c electrons shot towards the crack region between towers 3 and 4, in tower 4 but close to the tower 3 boundary and approximately towards the center of tower 4. (For details see table 5.4).

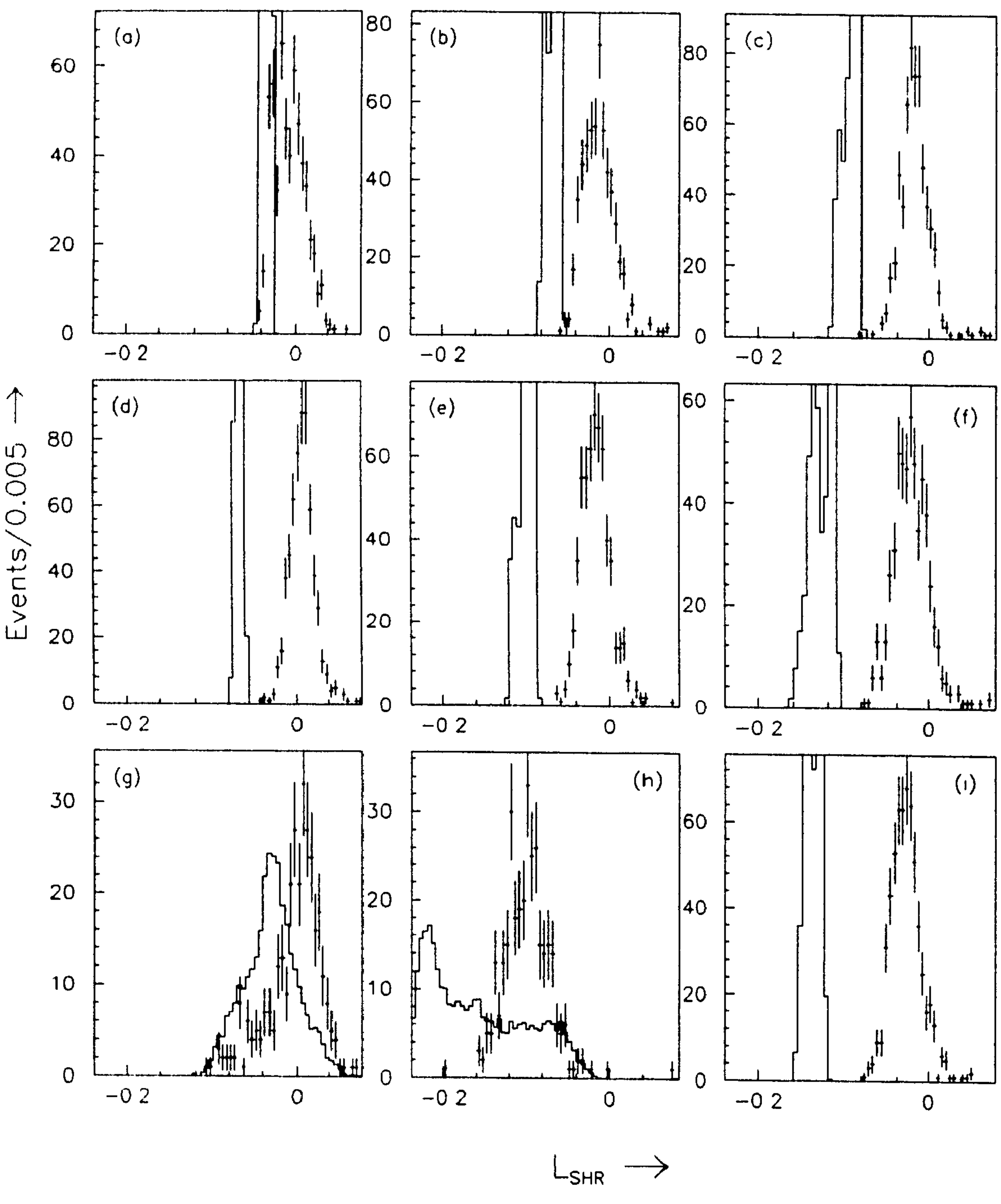

Figure 5.4: As in figure 5.3, but for the L_{SHR} variable.

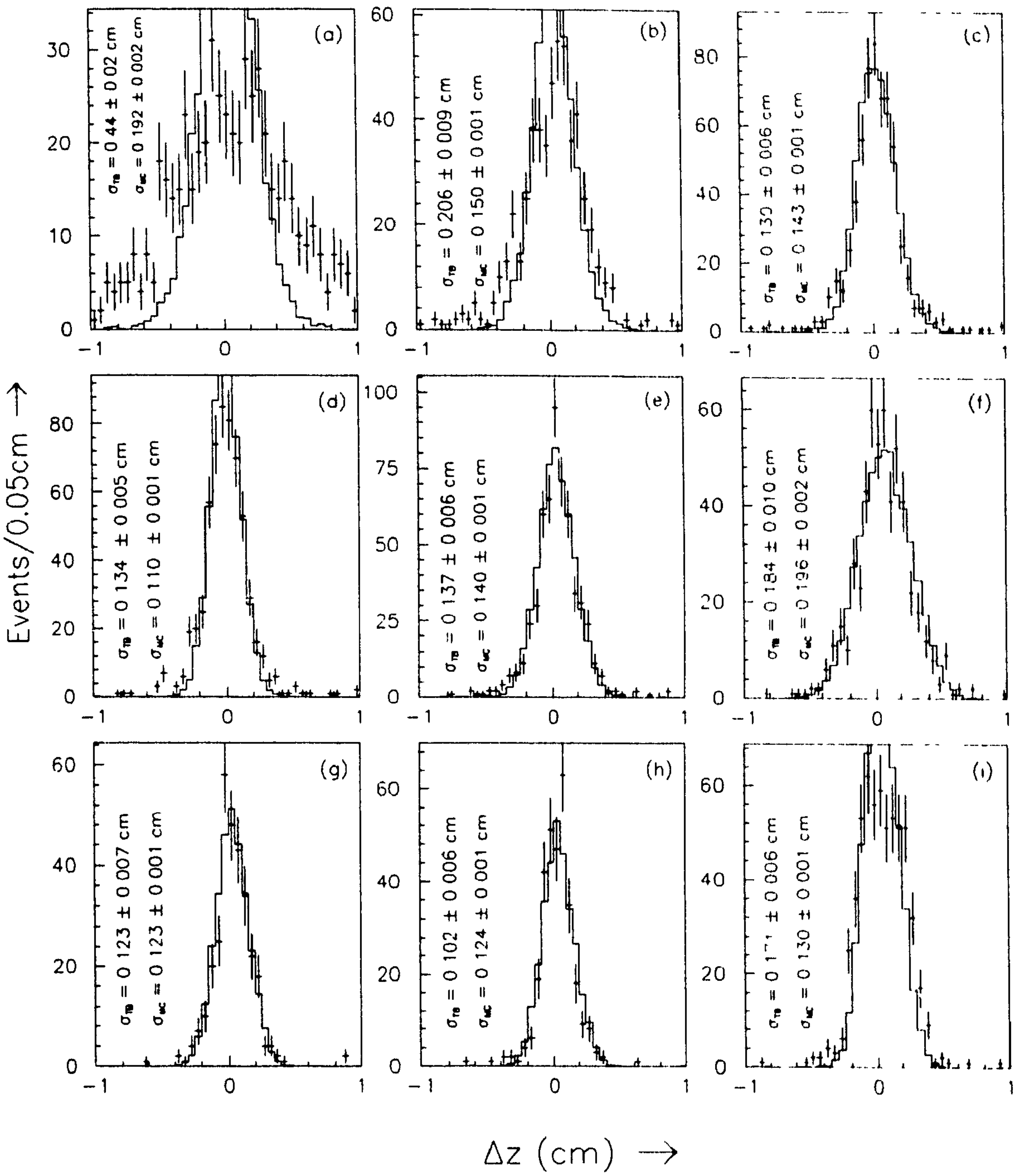

Figure 5.5: As in figure 5.3, but for the Δz variable.

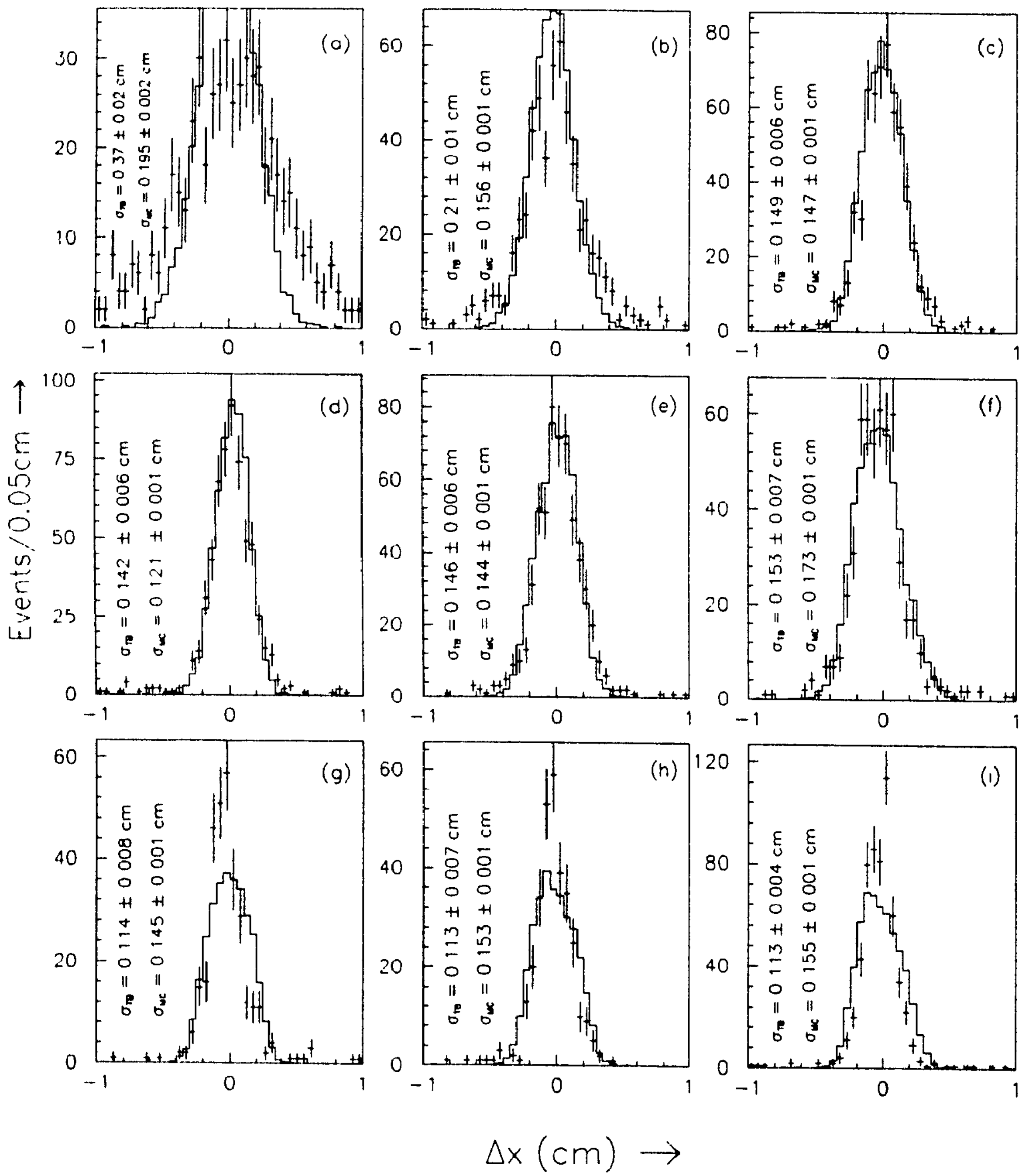

Figure 5.6: As in figure 5.3, but for the Δx variable.

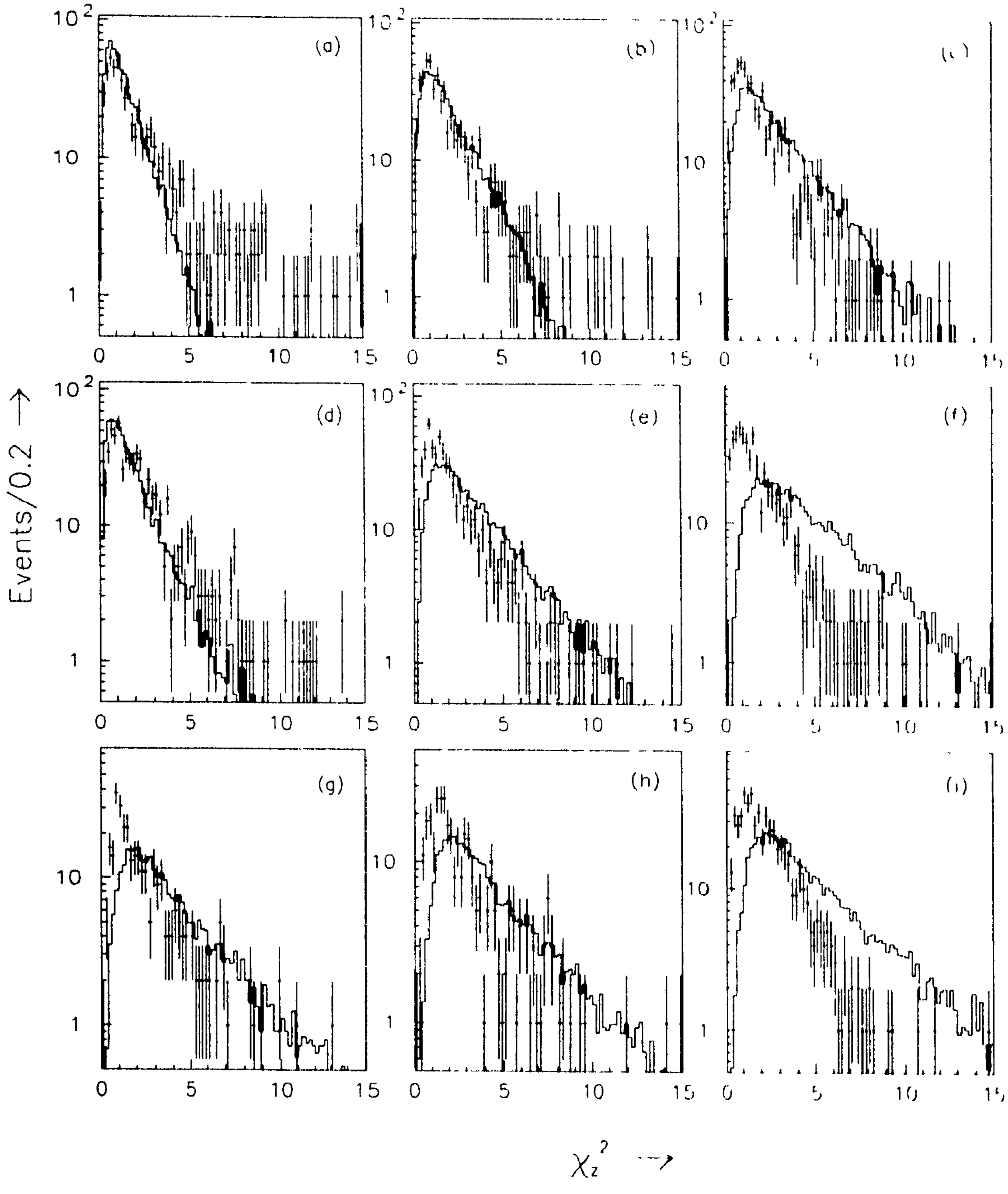

Figure 5.7: As in figure 5.3, but for the χ_z^2 variable.

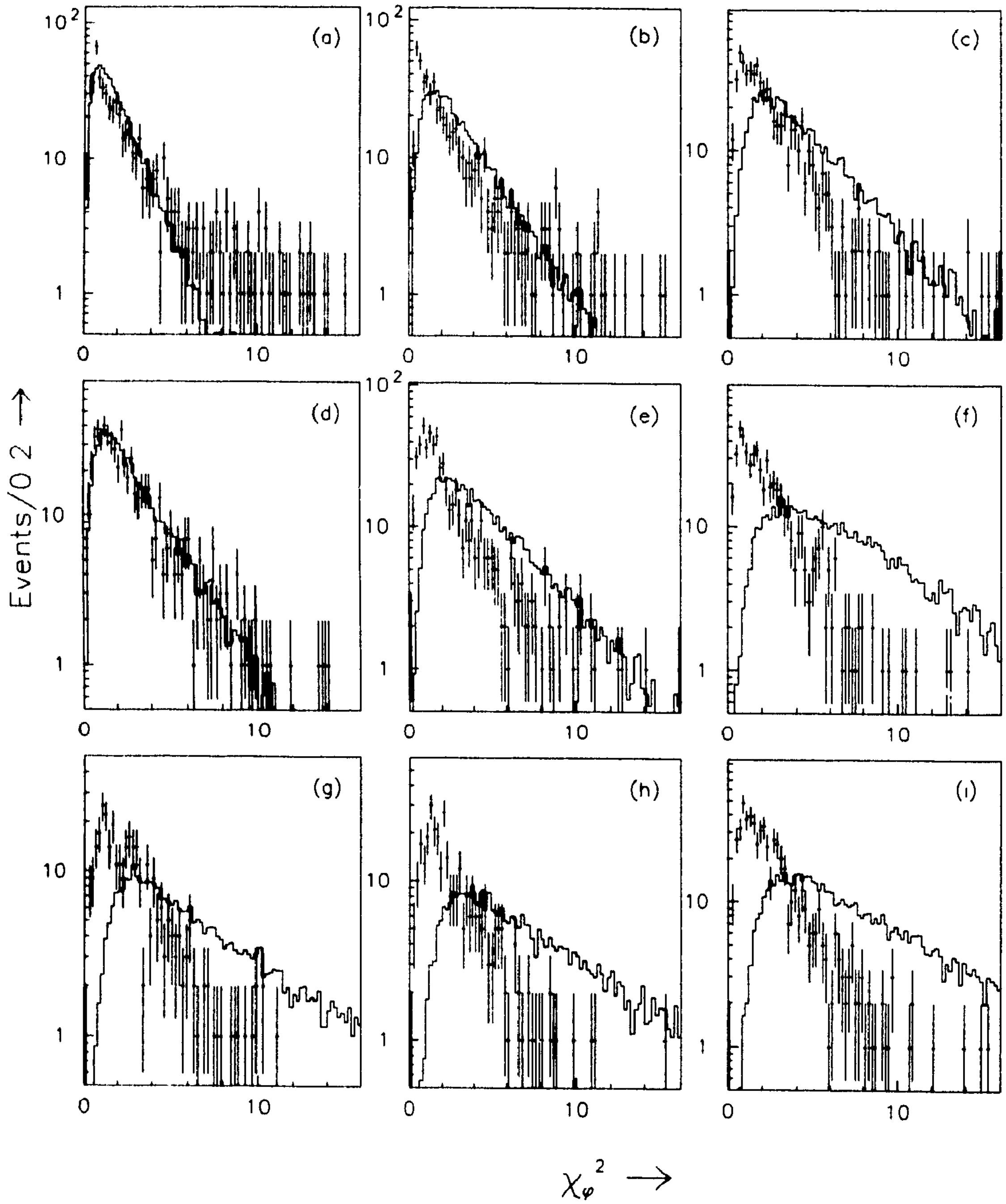

Figure 5.8: As in figure 5.3, but for the χ^2_ϕ variable.

particles are sufficiently close to the edges of the towers. This observation strengthens the hypothesis that the showers in the simulation are narrower than the test beam showers.

• Δz and Δx are Gaussians with the width decreasing as the energy increases for both the test beam and the Monte Carlo events. In a simple model we expect the sigmas of the Δz distributions to be[6]:

$$\sigma(\Delta z)_{TB} \approx \sqrt{\sigma_{CES}^2 + \sigma_{extrapolation}^2 + \sigma_{multiple\ scattering}^2} \tag{5.7}$$

$$\sigma(\Delta z)_{MC} \approx \sqrt{\sigma_{CES}^2 + \sigma_{multiple\ scattering}^2} \tag{5.8}$$

where "TB" stands for test beam, "MC" for Monte Carlo and the $\sigma_{extrapolation}$ is the uncertainty on calculations like those in section 3.2. Note that there is no uncertainty on the predicted hit position for the Monte Carlo events, since we know exactly where the particles are directed originally[7]. The sigma of the test beam data approaches the sigma of the Monte Carlo as the energy increases; from almost double at 10 GeV/c it becomes very similar at 50 GeV/c (see Fig. 5.5 and 5.6 (a), (b) and (c)). Note that the multiple scattering is different for the test beam setup and the CDF detector since the same amount of radiation lengths is spread in different ways between the test beam and CDF along the trajectory of the particle. This difference may be the cause why the test beam Δz and Δx distributions are much wider for 10 GeV/c electrons, whereas as the energy increases and the multiple scattering deviates the incoming particle less, the differences in sigmas become smaller. Note also that $\sigma_{CES} \sim \frac{1}{E}$ and $\sigma_{multiple\ scattering} \sim \frac{1}{P}$ [17], where E is the energy and P the momentum of the electron. So as the energy increases we expect the multiple scattering contribution to these sigmas to be much less than the CES resolution and since the CES resolution improves as the energy increases (see Fig. 2.2), we expect the sigmas of the Δz and Δx distributions to decrease as the energy increases. This appears to be the case, with the exception of the test beam Δz for $\approx$ 100 GeV/c electrons shot towards approximately the center of tower 4 (see Fig. 5.5 and 5.6 (a), (b), (c) and (i)). The fact that the test beam and Monte Carlo sigmas come very close to each other as the energy increases may imply that $\sigma_{extrapolation}$ is small.

The widths of the Δz distributions for both the test beam and the Monte Carlo events increase with the tower number (see Fig. 5.5 (d), (e) and (f)), which can

[6]Similar formulas for the Δx distributions can be written.

[7]We do not use the CTC to do the extrapolation of the electron tracks to the CES, since the magnetic field is switched off in the simulation, so as to match the test beam conditions, we make a straight line extrapolation.

be explained since the showers become more and more asymmetric as we move away from the $\theta = 90°$ plane because the more distant parts of the showers go through more material and they thus generate more ionization in the CES chambers (see Fig. 4.1 [22]). This asymmetry should not affect the x-direction measurement since the particles go through more or less the same x region. While this is the case for the test beam data, the Monte Carlo events give Δx distributions that become slightly wider as the tower number increases (see Fig. 5.6 (d), (e) and (f)).

It should be pointed out that the means of the gaussians do not agree for test beam and Monte Carlo events; this is due to a common offset in the test beam setup. We compare Δz and Δx by adjusting the test beam mean to the Monte Carlo mean.

• χ_z^2 and χ_ϕ^2 have a lack of events with low χ^2s and an excess for high χ^2s for the Monte Carlo electrons for momenta other than 10 GeV/c. This shift increases with the energy (see Fig. 5.7 and 5.8 (a), (b), (c) and (i)) and the tower number (see fig 5.7 and 5.8 (d), (e) and (f)), whereas it has a weaker dependence on the distance from the tower center (see Fig. 5.7 and 5.8 (g), (h) and (i)). Note that the agreement between test beam and Monte Carlo is best for ≈ 10 GeV/c where most of CDF data is. This could indicate that the parametrization of the shower profiles was done with low energy and small η test beam data (see eq. 4.2). Note nevertheless that the χ^2 cuts used to select electrons are $\chi^2 \lesssim 10$ to 12, and so the selection of electrons is not really affected by this discrepancy for towers 0 to 4 and energy less than 50 GeV/c.

5.4 An attempt to tune the Monte Carlo

It is apparent from the above comparison that the Monte Carlo reproduces the E_{CHA}/E_{CEM}, Δz and Δx variables quite well, it roughly reproduces the χ_z^2 and χ_ϕ^2 variables for electrons up to 50 GeV/c shot towards towers 0 to 4 [8], but it fails completely to reproduce the L_{SHR} variable. Since the highest discrepancies occur in the L_{SHR} variable, which is not reproduced by the Monte Carlo for electrons shot towards the center or close to the z boundaries of the towers, we look at this variable first.

The fact that L_{SHR} is not reproduced by the Monte Carlo in any of the cases examined indicates that the showers in the simulation are narrower than in the test beam data. As already said (section 4.3.2), in the CDFSIM Monte Carlo the transverse development of the shower is parametrized as two gaussians; a "narrow" and a

[8]Discrepancies are significant at higher energies and tower numbers.

"wide" component, where the narrow component carries 60 % of the energy and has $\sigma_{narrow} = (0.62 \pm 0.09)$ cm, whereas the wide component has $\sigma_{wide} = 2.21$ cm [9].

We tried to increase the widths of the wide and the narrow component of the showers, so as to have energy deposition in the neighbouring towers. For widths a factor of ≈ 2.2 larger than the ones currently used, the mean values of the L_{SHR} distributions agree. However, by making the showers wider, the agreement of the χ^2 distributions becomes worse; the shape for the Monte Carlo data becomes very different. On the other hand the χ^2 distributions can be made to give good agreement between test beam and Monte Carlo electrons if we make the showers a bit narrower; this can be done with sigmas ≈ 0.9 times the ones currently used in the simulation.

By feeding the narrow component of the showers with higher energy fractions, while having the sigma of the wide component of the showers about a factor of 2 to 3 times larger than those currently used, we lead the Monte Carlo χ^2 distributions towards lower values without destroying the agreement of the mean of the L_{SHR} distributions for 50 GeV/c electrons shot towards the center of tower 4 (see Fig. 5.9).

It appears that the χ^2 distributions and the L_{SHR} distributions cannot be optimized simultaneously using only the parameters discussed above. This means that there are other parameters that should be changed in order to have all of the variables to come to a good agreement between the test beam and the Monte Carlo. The tuning of the Monte Carlo is thus not straightforward and is currently under study.

[9]Both these sigmas are given here for the shower at the depth of the CES.

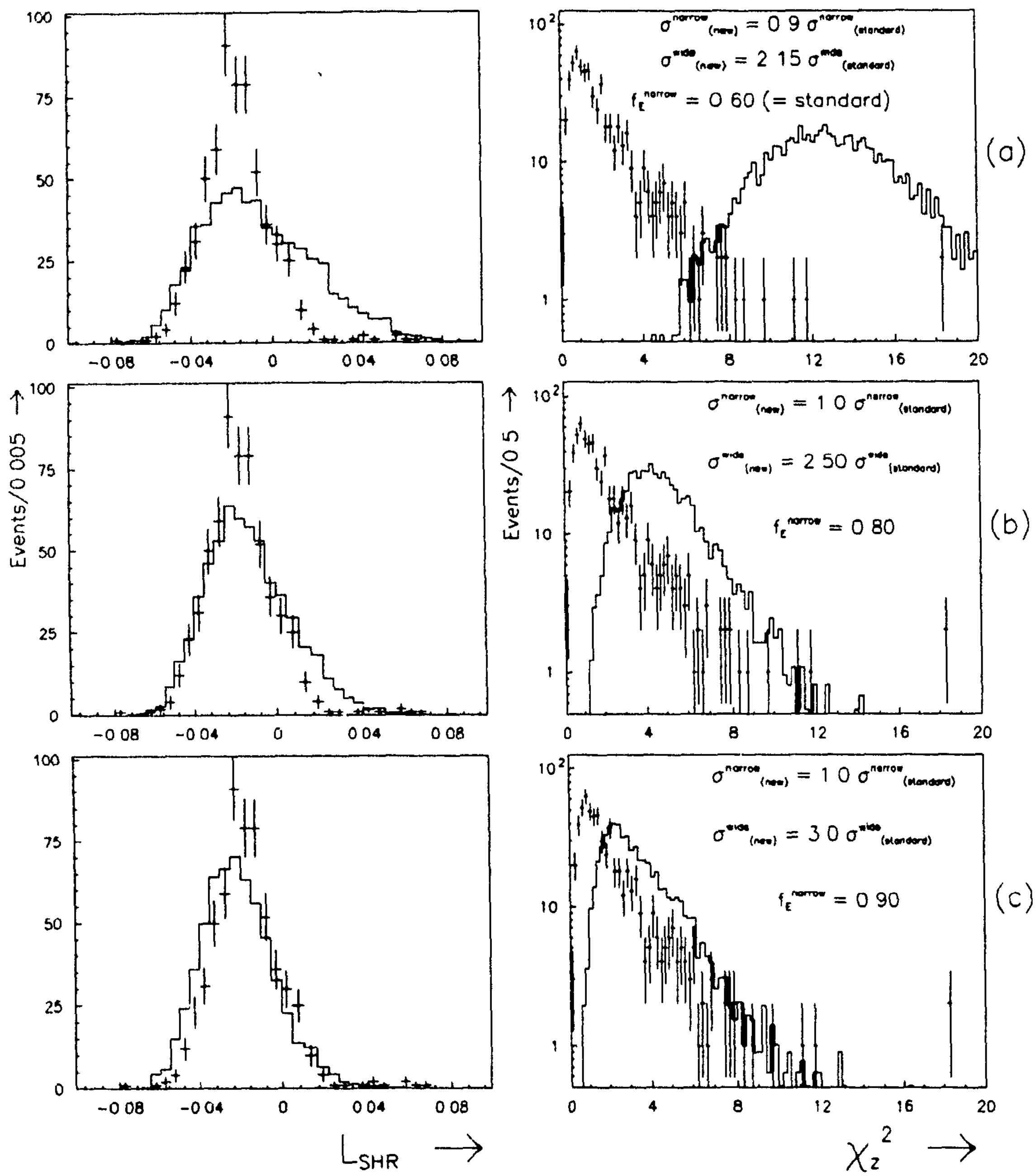

Figure 5.9: An attempt to bring both the L_{SHR} and the χ^2 distributions to an agreement between test beam and Monte Carlo, by varying the sigmas of the shower components and the energy fraction in the narrow component, for ≈ 50 GeV/c electrons shot towards the center of tower 4.

Chapter 6

Conclusion

A comparison of the CDF central calorimeter electron response between the 1991 test beam data and the CDF full detector simulation based on six variables used for electron identification was done. The comparison shows that the simulation reproduces the variables E_{CHA}/E_{CEM}, Δz and Δx quite well for all energies and towers. Variables χ^2_z and χ^2_ϕ are roughly reproduced for electrons up to 50 GeV/c shot towards towers 0 through 4 [1]. It fails however to reproduce the variable L_{SHR} (describing the lateral spread of the shower from the primary hit tower to neighbouring towers), because of the lack of energy deposited in those neighbouring towers. This problem seems to disappear if the energy deposited in the towers neighbouring the hit tower is ~ 1 % of the total energy.

The discrepancies between test beam and simulation can be reduced by varying some parameters in the CDF simulation. Although this has been demonstrated (see section 5.4 and Fig. 5.9), variations of one parameter affect more than one variable. This tuning is not straightforward and is currently under study.

[1] From $\theta_{CDF} \approx 90°$ to $\theta_{CDF} \approx 57°$.

Bibliography

[1] A. Bean *et al.*, Phys. Rev. D **35**, 3533 (1987).

[2] W. Bartel *et al.*, Phys. Lett. B **146**, 437 (1984).

[3] The CDF Collaboration, F. Abe *et al.*, Phys. Rev. D **45**, 3921 (1992).

[4] The CDF Collaboration, F. Abe *et al.*, Phys. Rev. Lett. **67**, 3351 (1991).

[5] The CDF Collaboration, F. Abe *et al.*, Phys. Rev. Lett. **68**, 3403 (1992).

[6] The CDF Collaboration, F. Abe *et al.*, Phys. Rev. Lett. **63**, 720 (1989).

[7] The CDF Collaboration, F. Abe *et al.*, Phys. Rev. D **43**, 2070 (1991)

[8] The CDF Collaboration, F. Abe *et al.*, Phys. Rev. Lett. **68**, 1104 (1992).

[9] The CDF Collaboration, F. Abe *et al.*, Phys. Rev. Lett. **62**, 3020 (1989).

[10] The CDF Collaboration, F. Abe *et al.*, Phys. Rev. Lett. **68**, 2734 (1992).

[11] The CDF Collaboration, F. Abe *et al.*, Phys. Rev. Lett. **67**, 2609 (1991).

[12] The CDF Collaboration, F. Abe *et al.*, Phys. Rev. Lett. **62**, 1825 (1989).

[13] The CDF Collaboration, F. Abe *et al.*, Phys. Rev. D **41**, 1717 (1990).

[14] The CDF Collaboration, F. Abe *et al.*, Phys. Rev. Lett. **63**, 1447 (1989).

[15] The CDF Collaboration, F. Abe *et al.*, Nucl. Instrum. Methods A **271**, 387 (1988).

[16] U. Amaldi, Physica Scripta. **23**, 409 (1981).

[17] Particle Data Group, *Review of Particle Properties*, Phys. Rev. D **45**, 11-II (1992).

[18] C. Fabjan, in *Experimental Techniques in High Energy Physics*, edited by T. Ferbel. Addison-Wesley, Menlo Park CA (1987)

[19] J. Freeman, *Description of the CDF Calorimetry Simulation*. CDF internal note (1985).

[20] L. Balka *et al.*, Nucl. Instrum. Methods A **267**, 272 (1988).

[21] S. Bertolucci *et al.*, Nucl. Instrum. Methods A **267**, 301 (1988).

[22] R. Harris, *Definition of CES* χ^2. CDF-Note 1329 (1991).

[23] The CDF Collaboration, F. Abe *et al.*, Phys. Rev. D **45**, 3921 (1992).

[24] S. Kopp, CDF-Note 1689 (1991).

[25] S.R. Hahn *et al.*, Nucl. Instrum. Methods A **267**, 351 (1988).

[26] P. Maas, private communication.

[27] P. Maas, *Momentum Determination at the 1990 CDF Testbeam*. CDF-Note 1339 (1990).

[28] J. Freeman, *Description of the CDF Detector Simulation Programm CDFSIM*. CDF internal note (1985).

[29] S. Bertolucci *et al.*, *Comparison of Hadronic Shower Monte Carlo Simulation and Test Beam Data*. CDF-Note 290 (1985).